AIAA JOURNAL
Vol. 56, No. 5, May 2018

Optimization and Validation of Cycloturbine Blade-Pitching Kinematics via Flux-Line Theory

Zachary Adams* and Jun Chen†
Purdue University, West Lafayette, Indiana 47907

DOI: 10.2514/1.J056575

The newly developed flux-line theory identifies the maximum power harvested by a cycloturbine and the associated fluid–turbine interaction pattern. This work designs blade-pitching functions that maximize turbine power by identifying the blade lift coefficient functions required to optimally decelerate the flow, relating these waveforms to blade angle of attack functions through a novel semi-empirical curvilinear flow aerodynamics model, and finally computing optimal blade-pitch motions with freestream flow data from flux-line theory. At low and moderate tip speed ratios, the blades stall before achieving the required deceleration force. In those cases, more wind power is extracted by braking the flow through both the upstream and downstream portions of the cycloturbine. In a truck-mounted cycloturbine test, the flux-line optimal pitching kinematics outperformed sinusoidal and fixed-pitching kinematics. The turbine achieved a mean gross aerodynamic power coefficient of 0.44 (95% confidence interval: [0.388, 0.490]) and 0.52 (95% confidence interval: [0.426, 0.614]) at design tip speed ratios of 1.5 and 2.25, respectively, which exceeds all other low tip speed ratio vertical-axis wind turbines. Two-dimensional Reynolds-averaged Navier–Stokes simulations show that the optimal blade-pitching functions achieve high power coefficients by evenly extracting energy from the flow without blade stall or detached turbine wakes.

Nomenclature

A_d	=	simplified constant value of deceleration along downstream flux line [$a_d(s)$ becomes the constant A_d]
A_u	=	simplified constant value of deceleration along upstream flux line [$a_u(s) = A_u$]
$\mathcal{AR}$	=	blade aspect ratio
a_d	=	downstream flux-line inflow factor
a_u	=	upstream flux-line inflow factor
b	=	blade span
c	=	blade chord
C_{D_o}	=	parasite drag coefficient
C_D	=	coefficient of drag (three-dimensional)
C_l	=	coefficient of lift (two-dimensional)
C_L	=	coefficient of lift (three-dimensional)
C_{L_o}	=	zero angle of attack lift
C_{L_α}	=	blade lift-curve slope
C_p	=	coefficient of power
D/L	=	blade drag-to-lift ratio
e	=	Oswald efficiency factor
$f_\parallel$	=	force per unit area flux line that stream tube exerts on blade parallel to streamline
$f_\parallel$	=	force per unit area flux line that stream tube exerts on blade perpendicular to streamline
k	=	reduced frequency
n	=	number of blades
P	=	pressure
P_∞	=	freestream pressure
Re	=	Reynolds number
r	=	rotor radius
s	=	streamline index
U	=	component of fluid velocity parallel to the direction of freestream flow
U_∞, V_∞	=	freestream velocity
V_d	=	induced velocity through the downstream flux line/rotor
V_r	=	flow velocity relative to blade
V_u	=	induced velocity through the upstream flux line/rotor
x	=	Cartesian coordinate parallel to the direction of freestream flow
y	=	Cartesian coordinate perpendicular to the direction of freestream flow
z	=	Cartesian coordinate along rotational axis of cycloturbine
α	=	blade angle of attack
γ	=	angle between rotor flux line and streamline
$\Delta\alpha_{L_{vi}}$	=	change in angle of attack from virtual incidence
$\Delta\alpha_{vi}$	=	virtual incidence angle
$\Delta C_{D_{cf}}$	=	drag due to curvilinear flow
$\Delta C_{D_{vc}}$	=	change in drag coefficient from virtual camber
$\Delta C_{L_{vc}}$	=	virtual camber coefficient
$\Delta C_{L_{vc}}$	=	change in lift coefficient from virtual camber
ζ	=	angle between streamline and flow velocity relative to blade
θ	=	blade pitch
κ	=	angular flow distribution parameter
λ	=	tip speed ratio
ν	=	kinematic viscosity
ρ	=	fluid density
σ	=	rotor solidity
ϕ	=	cyclic position around the rotor
ψ	=	curvilinear flow effectiveness factor
Ω	=	rotational speed

Received 28 July 2017; revision received 5 December 2017; accepted for publication 5 December 2017; published online 28 February 2018.

*Ph.D. Graduate, School of Mechanical Engineering; zachary.adams.13@us.af.mil.

†Associate Professor, School of Mechanical Engineering; junchen@purdue.edu.

I. Introduction

CYCLOTURBINES are a subset of the H-bar type vertical-axis wind turbines (VAWTs) that are designed to vary the blade-pitch angle throughout each revolution to extract the maximum energy from the wind. Cycloturbines and other VAWTs could enable renewable power generation in new locations. The heavy generator and gearbox are positioned at the bottom of the machine, which lowers their center of gravity and facilitates positioning on a floating platform [1,2]. Such turbines could access the wind resources in the deep water off coastlines adjacent to population centers. On land or water, the individual turbine land-specific power density is greater for VAWTs than horizontal-axis wind turbines (HAWTs), whose height

can be extended to capture more wind without requiring a larger footprint [3,4] and which can capture energy lost by HAWTs when the wind direction shifts quickly [5].

Despite these and other advantages, most present VAWTs use immovable blades that produce power only during a small portion of their revolution and otherwise are stalled or consume generated power. These fixed-pitch VAWTs achieve low power coefficients and experience high cyclic aerodynamic vibrations that reduce mechanical life [3,6,7]. Moreover, aerodynamic forces are insufficient to initiate turbine rotation, and so a separate motor must be employed [3,5]. Cycloturbines bypass these problems by cyclically actuating the blades throughout the revolution, as shown in Fig. 1. Several studies demonstrated that cycloturbines are self-starting and produce more power than fixed-pitch VAWTs [3,5,8].

Designers must select proper blade-pitch motions to maximize cycloturbine performance. Optimizing blade-pitching functions is challenging due to turbine–fluid interaction and complex blade aerodynamics. As the cycloturbine extracts power, the wind is braked and expands. Momentum theories easily handle this expansion for HAWTs because the fluid expands through a perpendicular rotor disk. For VAWTs, the flow widens through the middle of the circular cross section, which changes the relative flow angle and the forces on the blades as well as the global flow pattern. Furthermore, the curvilinear, unsteady, centrifugally loaded blade flow environment prevents the application of traditional aerodynamic expressions to relate blade angle of attack to lift and drag coefficients. To an observer fixed to the rotating blade, centrifugal force imposes a pressure gradient on the blade boundary layer. This gradient decreases the maximum positive stalling angle of attack and increases the maximum negative stalling angle of attack by enhancing boundary-layer attachment and separation on the interior and exterior faces of the turbine blades, respectively [9]. Unsteady aerodynamics are a major feature of the rapidly pitching blades. In the extreme, an inverse Kármán vortex sheet rolls down the blade from leading edge to trailing edge, and the low-pressure region delays separation and enhances lift during its passage [10]. Most significantly, cyclorotor and cycloturbine blades experience a chordwise variation in the rotational component of velocity known as curvilinear flow. This chordwise velocity difference results in a flow pattern and blade pressure distribution different from that experienced in a wind-tunnel setting. Cycloturbine blade lift, drag, and moment coefficients cannot be accurately predicted with the traditional expressions (i.e., $C_L = \alpha C_{L_\alpha} + C_{L_o}$, and $C_D = C_{D_o} + C_L^2/e\pi\mathcal{R}$) used on design of aircraft, HAWTs, propellers, and helicopter rotors. Thus far, the combination of complex flow and experimental barriers to fundamental research impeded the development of a well-accepted method for accurately modeling blade lift, drag, and moment characteristics of cycloturbines.

To design a highly efficient cycloturbine, the ideal blade pitch θ must be specified as a function of the cyclic blade position ϕ, tip speed ratio (TSR) λ, and cycloturbine geometry, namely rotor solidity $\sigma = nc/2\pi r$ [i.e., $\theta(\phi, \lambda, \sigma)$]. Several researchers sought this optimal function. In 1978, Healey suggested that VAWT blade lift and drag coefficients could be adjusted to produce the induced velocity across a horizontal-axis turbine operating at the Betz limit [11]. This innovative inverse method does not excessively slow the wind by maximizing torque. However, his underlying model was primitive, and the insight of using an inverse method has not been applied to cycloturbines since [11]. Instead, researchers parametrically evaluated pitching motions and applied optimization algorithms. In 1987, Vandenberghe and Dick evaluated second-order harmonic sinusoidal pitching kinematics but did not address the need to vary pitch functions with TSR [12].

Nearly two decades later, Paraschivoiu et al. [8] coupled a genetic algorithm with an existing double multiple stream-tube blade-element model, which does not account for flow expansion with deceleration, to optimize pitching motions at a high TSR. The algorithm sought maximum blade torque throughout the revolution and was restricted to small pitch angles, but it suggested an annual energy improvement of 30% over fixed-pitch motions [8]. In 2012, Rathi implemented a similar torque maximization algorithm on a multiple double stream-tube blade-element momentum model [13]. His model suggested that these pitching motions would only exceed the fixed-pitch efficiency for low TSRs. Paraschivoiu et al. and Rathi overlooked Healey's prior conclusion that maximizing torque on a model without capturing flow expansion will not maximize total turbine power.

Other researchers explored optimal pitch through parametric experimental studies. In 1980, Brulle electrically actuated a precomputed maximum high or maximum low angle of attack on a McDonnell Aircraft 40 kW cycloturbine but achieved less than expected performance [14]. In 2011, Erickson et al. found that a 9 deg sinusoidal pitching amplitude maximized performance in a parametric wind-tunnel study [15]. In a 2013 high-solidity cycloturbine wind-tunnel study, Benedict et al. achieved a maximum coefficient of power of 0.31 with a 25 deg amplitude pitching [3].

These parametric studies are convincing but inherently limited to the attainable pitch motions prescribed by the pitching mechanism implemented. This reduces the number of pitch design variables and makes a parametric study tractable. However, optimal blade-pitch functions could be quite different from those attainable with simple blade-pitch mechanisms. Recently, flux-line theory, a novel momentum type model for cycloturbines and cyclorotors that captures flow expansion and bending within the turbine, was developed [16]. This theory describes the optimal flow and turbine flow interaction. More specifically, flux-line theory identifies the inflow factors $a_u(s)$ and $a_d(s)$ that determine how the blades should decelerate the freestream flow for maximum turbine power. However, that work did not connect these optimal flow conditions to actual blade-pitching kinematics.

This paper proposes a multistep inverse method to optimize blade-pitching functions and compares those motions to sinusoidal and fixed-pitch kinematics with a medium-scale truck-mounted cycloturbine experiment and two-dimensional (2-D) Reynolds-averaged computational fluid dynamics (CFD) simulation. Section II reviews the key elements and conclusions of flux-line theory, and Secs. III and IV detail the experiment and CFD simulation respectively. Section V presents the inverse method to predict blade pitch. Section V.A derives the required blade lift and drag characteristics to attain the optimal inflow factors. Once identified, these coefficients must be recast in terms of blade angle of attack and blade pitch for a specific turbine geometry. Section V.B introduces a novel semi-empirical method to model curvilinear flow blade lift and drag coefficients for a particular cycloturbine geometry. Because cycloturbine blades stall,

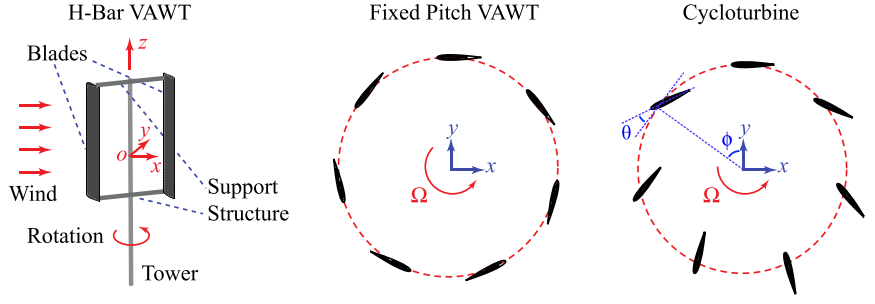

Fig. 1 Schematics of H-bar type VAWT and comparisons of fixed-pitch and cycloturbine (variable-pitch) variants.

they cannot always produce the lift coefficients required to attain optimal flow as predicted by flux-line theory. Under certain operating conditions, more power can be obtained by operating the turbine under nonoptimal flow conditions. These dual-deceleration schemes are explained in Sec. V.C. Together, these relationships enable computation of the optimal pitching motion [i.e., the optimal $\theta(\phi, \lambda, \sigma)$], as described in Sec. V.D. Sections VI and VII compare the experimental and CFD results from various pitch motions. Section IX summarizes the discoveries and provides future recommendations.

II. Flux-Line Theory Summary

Flux-line theory is a newly developed low-order model for analyzing cycloturbines and cyclorotors [16]. This theory models the location of flow streamlines as they enter and exit a two-dimensional cycloturbine. This flow information is used compute the power produced and forces placed on that cycloturbine. Figure 2 describes the central nomenclature and geometry of the theory. The flow velocity and direction along a streamline are characterized at four locations where a "flux line" crosses the streamline. These are 1) freestream flux line (denoted by subscript ∞) at a far upstream location unaffected by the turbine; 2) upstream flux line (denoted by subscript u), where flow passes into the turbine; 3) downstream flux line (denoted by subscript d), where the streamlines exit the rotor; and 4) wake flux line (denoted by subscript w), at the far wake. The streamlines are labeled by a streamline coordinate s, whose value ranges from 0 to 1, spanned by the two streamlines that pass just tangent to the top and bottom of the rotor disk. After the flow characteristics at the flux lines are computed, the Cartesian location of the streamlines is calculated as well as the power, lift, and drag on the turbine.

Flux line predicts the nondimensional turbine power as

$$C_p = 4\left(\frac{1}{2r}\frac{dy_\infty}{ds}\right)\left[\int_0^1 a_u(s)(1-a_u(s))\,\mathrm{d}s + \int_0^1 (1-2a_u(s))^2 a_d(s)(1-a_d(s))\,\mathrm{d}s\right] \tag{1}$$

where the integral sum term estimates the mass specific momentum exchange between the flow and the turbine. The factor

$$\frac{1}{2r}\frac{dy_\infty}{ds} = \frac{\pi}{\int_0^1 (V_\infty/V_u(s)\sin(\gamma_u(s)))\,\mathrm{d}s + \int_0^1 (V_\infty/V_d(s)\sin(\gamma_d(s)))\,\mathrm{d}s} \tag{2}$$

determines the proportion of freestream mass decelerated by the turbine. The inflow functions $a_u(s)$ and $a_d(s)$ describe the deceleration for the flow along the upstream and downstream flux lines. These are related to the velocity along each flux line by

$$V_u(s) = V_\infty(1-a_u(s)) \tag{3}$$

and

$$V_d(s) = V_\infty(1-2a_u(s))(1-a_d(s)) \tag{4}$$

The angles γ_u and γ_d at which the flow crosses the upstream and downstream flux lines are modeled by the two-parameter $\epsilon - \eta$ submodel [16].

Flux-line theory identifies the optimal inflow factor functions $a_u(s)$, and $a_d(s)$ for maximum power generation [16]. It suggests the

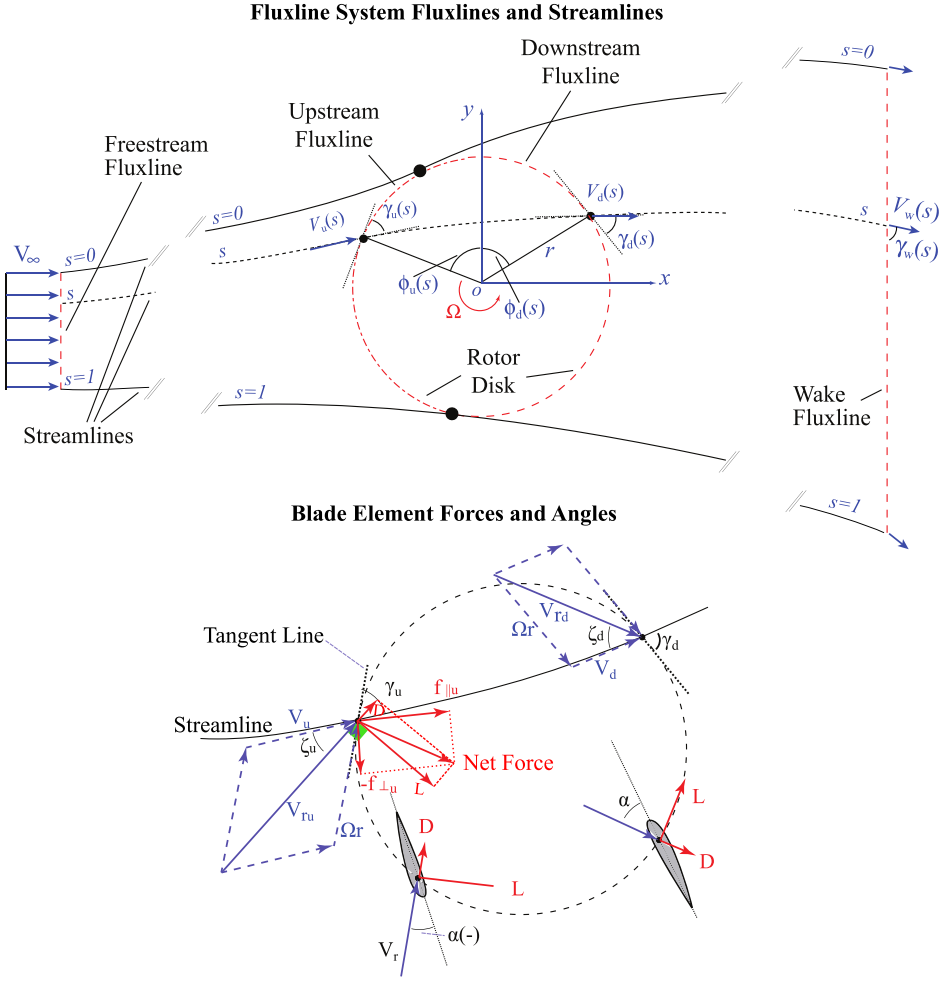

Fig. 2 Schematic of flux-line model: system, geometry, and variables.

upstream flux line should not decelerate the flow [$a_u(s) = 0$], whereas downstream flux-line deceleration should vary with streamline coordinate but generally falls near one-third [$a_d(s) \approx 1/3$] [16]. This paper extends that analysis to predict attainable blade-pitch motions and evaluate those motions with an experiment and CFD.

III. Experimental Setup

To experimentally evaluate the improved blade-pitching kinematics, a three-bladed cycloturbine was designed. The turbine characteristics are summarized in Table 1 and the setup is depicted in Fig. 3. The scale of the turbine was selected to ensure a sufficiently large operating Reynolds number such that the results are applicable to a large household through utility-scale power-generating turbines. Under all circumstances, the turbine Reynolds number (defined as $Re = (cV_\infty\sqrt{1+\lambda^2})/\nu$) was greater than 100,000.

Three blades with NACA 0012 airfoil sections were selected to minimize aerodynamic interference without undue vibration due to cyclic aerodynamic variations and to be consistent with previous experiments by Madsen and Lundgren [17] as well as Vandenberghe and Dick [12,18]. The high solidity of 0.2 was selected to decrease the required TSR to attain high power coefficients without causing cascade blade interference effects. The blades were manufactured via a foam and fiberglass lay-up over aluminum cylindrical spars.

The spoke structures shown in Fig. 4 support the top and bottom of these blades. The upper spoke supports the blade via an aluminum–cherry wood sandwich structure. The lower spoke supports the blades via a monocoque aluminum structure concealing an internal mechanism to control blade pitch. A bellcrank mechanism connects to the blades via a D-profile shaft. A cam bearing on the opposite side of the bellcrank determines blade pitch by radial cam displacement. The cam bearing is drawn outward on the inside of a cam by centrifugal force and spring tension.

This mechanism can achieve any blade-pitching motion with different cam shapes. Five two-dimensional aluminum cams were machined to test particular operating points. A circular cam allows testing of traditional fixed-pitch (when centered on the axis of rotation) and sinusoidal pitch waveforms (when the center of the cam is offset from the axis of rotation). Cams were also milled with the optimal shape developed in Sec. V for TSRs of 0.5, 1.5, 2.25, and 3. Although these cams were developed for a particular TSR, they were tested both at the design TSR ("on design") and at adjacent TSRs ("off design"). Of the flux-line optimal cams, only those at a TSR of 1.5 and 2.25 produced viable results. The 0.5 TSR cam pushed the cam bearings to the minimum and maximum displacement during each revolution and was not tested at full design speed for fear of damage to the experiment. The 3.0 TSR cam was experimentally evaluated, but because the rotational speed of the tests was limited, its design point occurred at a low wind speed where measurement errors were prohibitively high.

A larger concentric stationary aluminum shaft with bearings on either end supports the turbine shaft. A shaft collar beneath the lower bearing maintains rotating shaft orientation. A keyed adapter connects this shaft to an 113 N · m (1000 in.·lb) Sensor Developments shaft-to-shaft torque cell and an optical encoder (to measure rotational speed). As shown on the right of Fig. 3, a 7.5 hp three-phase ac induction motor brakes, or drives, the turbine through the 5:1 reduction pulley system. A motor–generator is required to both drive the rotor to determine aerodynamic and frictional power losses as well as brake the turbine as it extracts energy from the wind. A Yaskawa GPD 315/V7 7.5 kW (10 hp) variable-frequency drive controls the speed of the motor–generator and therefore turbine. Signals from the torque cell are low-pass filtered, digitized, and sampled by a data acquisition system. A Davis Instruments wireless weather station records atmospheric conditions including wind direction, speed, temperature, pressure, and humidity. Labview software records all data.

Table 1 Experimental conditions

Category	Value
Radius r	0.686 m (2.25 ft)
Span b	1.372 m (4.5 ft)
Chord c	0.287 m (0.94 ft)
Solidity $\sigma = nc/2\pi r$	0.2
Chord-to-radius ratio c/r	0.418
Blade aspect ratio b/c	4.781
Blade airfoil	NACA 0012
Number of blades (n)	3
Pitching axis location	25%c
Freestream velocity V_∞	0–7 m/s
Tip speed ratio λ range	0–3
$Re = (cV_\infty\sqrt{1+\lambda^2})/\nu$	130,000–440,000
Experimental conditions	Open air (vehicle mounted)

The setup was mounted on a truck to generate the wind independent of environmental conditions. This process permits testing at large Reynolds numbers without the use of enormous wind tunnels or prohibitively high rotational speeds. Although this approach eliminates wind-tunnel wall effects and provides a comparable turbulence level to stationary turbines, the truck could distort the flowfield, and it is more difficult to control the wind speed precisely. These problems were addressed via additional testing and a robust test procedure.

The flowfield of this truck was first evaluated by vertically traversing a single-component hot-wire anemometer at different locations along the width of the vehicle. As shown in Fig. 5, the velocity above the cab (well below the bottom of the test cycloturbine) quickly approaches a freestream value, which is consistent at locations along the vehicle width. The direction of the wind velocity was visualized with an array of strings mounted throughout the test space. This string array was moved forward and aft in the truck bed, and a high-speed camera recorded the orientation of the strings. Inspection of the high-speed videos showed that the strings remained parallel with the longitudinal axis of the truck and displayed a consistent turbulence level. Precise control of the wind velocity above the truck is difficult because the truck road speed cannot be adjusted quickly enough to account for ambient wind variations. Consequently, the cycloturbine was tested by slowly accelerating and decelerating the truck while continuously measuring the wind velocity. Because the time scale of the change in wind speed (0.35 m/s^2) is much smaller than the tip speed of the turbine (14.4 m/s), this procedure establishes a quasi-steady measurement at a spectrum of wind velocities.

IV. Computational Methods

By design, flux-line theory is a simplified model that neglects unsteady fluid flow and blade interference. These phenomena, inherent to cyclorotors and cycloturbines, are arduous to pinpoint experimentally. Jarugumilli [19] and Benedict et al. [3] showed that 2-D CFD provides qualitative insight into the flow passage through cyclorotors in forward flight and a quantitatively accurate computation of the coefficient of power for a low TSR wind turbine. This study applies CFD to qualitatively examine the difference in the flowfields for different blade-pitching motions.

A. Grid Generation

Grid generation software was developed to produce 2-D structured grids around cycloturbines with various numbers of blades, airfoils, solidities, and radii. These meshes use a sliding interface for the rotor and each of the blades to allow the blades to rotate about the rotor and pitch simultaneously. Computation between the sliding domains is accomplished by local Galerkin projection and is referred to as a cyclic arbitrary mesh interface (AMI) [20], as shown in Fig. 6. Cells adjacent to these interfaces are comparable in size with an aspect ratio near unity to minimize computational errors. Relative cell density elsewhere was designed to parallel the anticipated scale and complexity of flow structures. A mesh refinement study evaluated the required cell density. The optimized blade-pitch motion with the experimental geometry and a TSR of 3 was selected as the refinement study case to minimize variation due to turbulent separation during blade stall. The left panel of Fig. 7 plots the coefficient of power

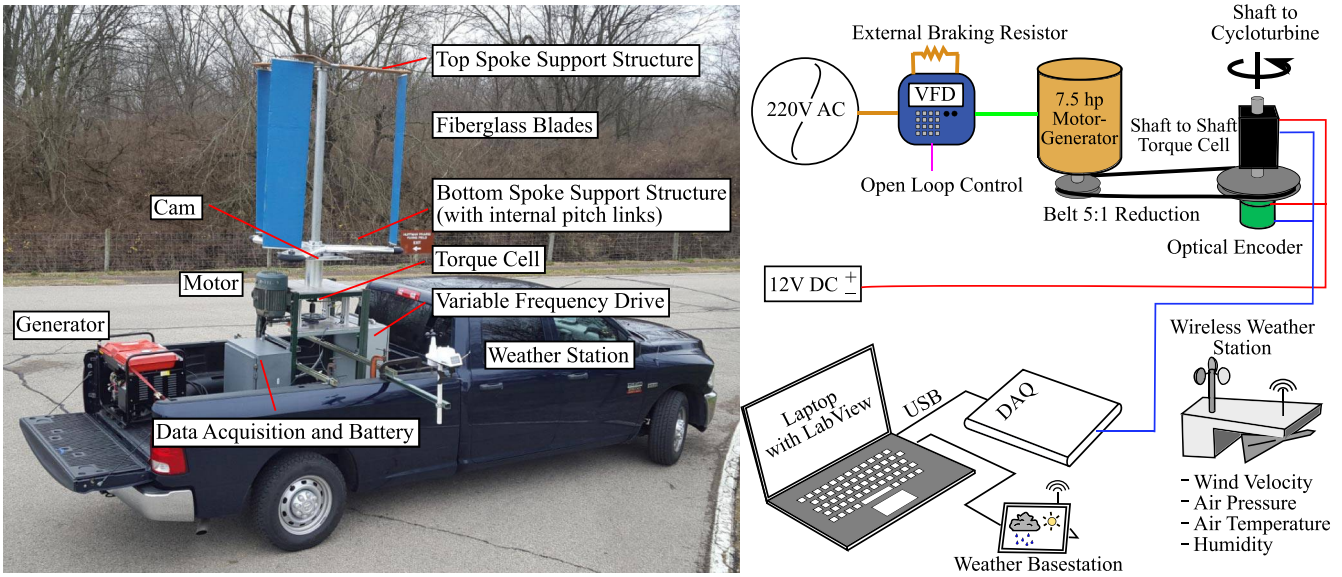

Fig. 3 Overview of experimental cycloturbine mounted in truck bed (left), and schematic of turbine power dissipation, control, and instrumentation system (right).

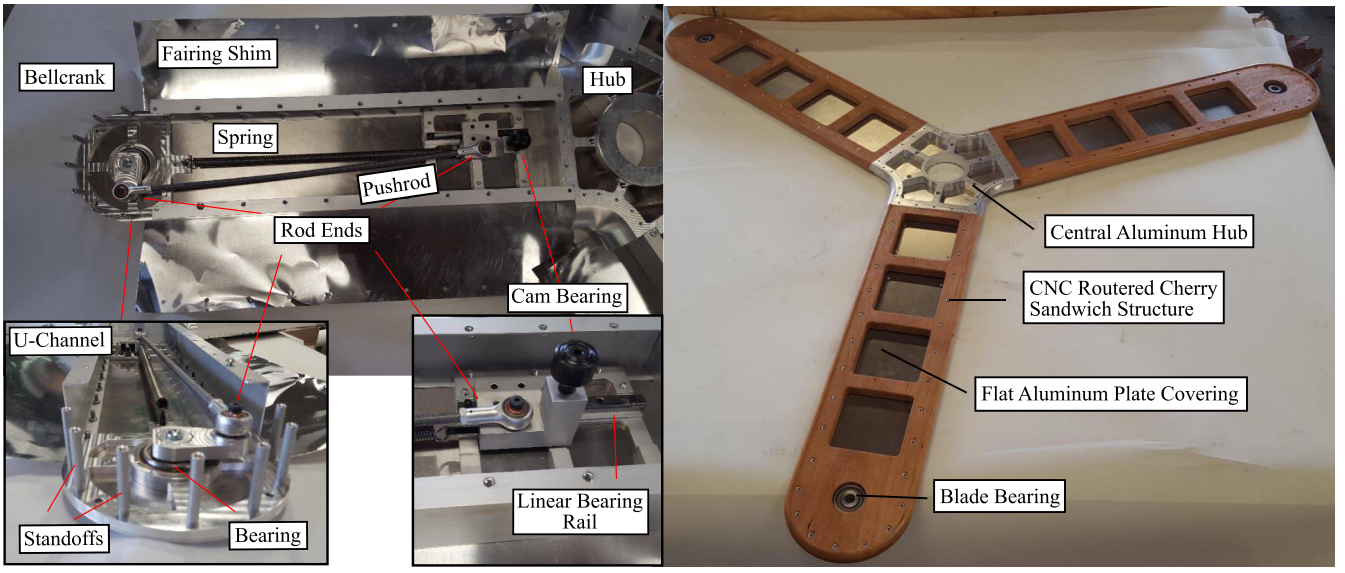

Fig. 4 Top spoke with half of aluminum outer plating removed to reveal computer numerical control (CNC) milled cherry inner sandwich structure.

contribution by a single blade as a function of cyclic location around the turbine for six meshes of increasing cell count. For the majority of the revolution, the results converge when the number of cells reaches 300,000. To ensure accuracy, the next denser grid (408,216 hexahedral cells) was selected for further studies. The cell maximum cell expansion ratio from the blade surface is 1.011 with a maximum aspect ratio of 29.5 and a first cell y^+ distance of 30.8. Local Galerkin projection (cyclic AMI) [20] handles the cyclic AMI boundary.

B. Flow Solver

The open-source CFD software openFoam was implemented as the Reynolds-averaged Navier–Stokes (RANS) solver. An incompressible combined transient SIMPLE (from "semi-implicit method for pressure linked equations") PISO (from "pressure implicit separating of operators") algorithm was applied, which provides high stability and diminishes computation time by permitting larger time steps [21]. Blade motion does not numerically distort the solution because the greatest time step during steady-state turbine operation corresponds to only 0.097 deg of turbine revolution. An incompressible solution is justifiable because there is no heat added to the flow, and the highest encountered speed is 12 m/s, or only 3.4% of the speed of sound under sea-level standard conditions.

The k–ϵ and k–Ω shear-stress transport (SST) turbulence models were evaluated for RANS closure, as shown in Fig. 7. The predictions from the k–Ω SST model agree better with experimental data. This echoes Chowdhury et al.'s recent assessment that k–Ω SST is the best turbulence model for VAWTs in their comparison of three-dimensional RANS simulations of a fixed-pitch turbine [22]. A far-field turbulence intensity of 5% was prescribed as the turbulent inlet conditions. This represents the lower limit of turbulence on large wind farms in offshore conditions and is a minimum turbulence scenario for any wind turbines [23]. Wall functions were prescribed on the blade surfaces to model the turbulent layers near the surface without the need for extraordinarily small computational cells.

C. Validation

The right panel of Fig. 7 compares the numerical predictions to the Vandenberghe and Dick outdoor cycloturbine experiment [12,18]. Both k–ϵ and k–Ω SST capture the general trend and magnitude of the

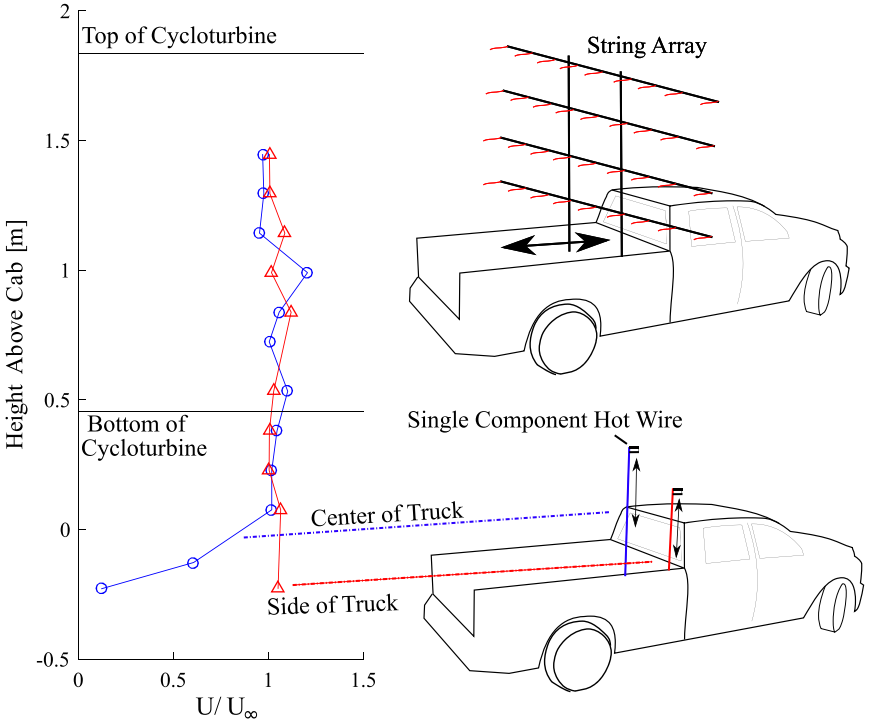

Fig. 5 Hot-wire velocity measurement above pickup truck cab (left), and drawing of qualitative string analysis of wind direction and turbulence intensity and hot-wire measurement tests (right).

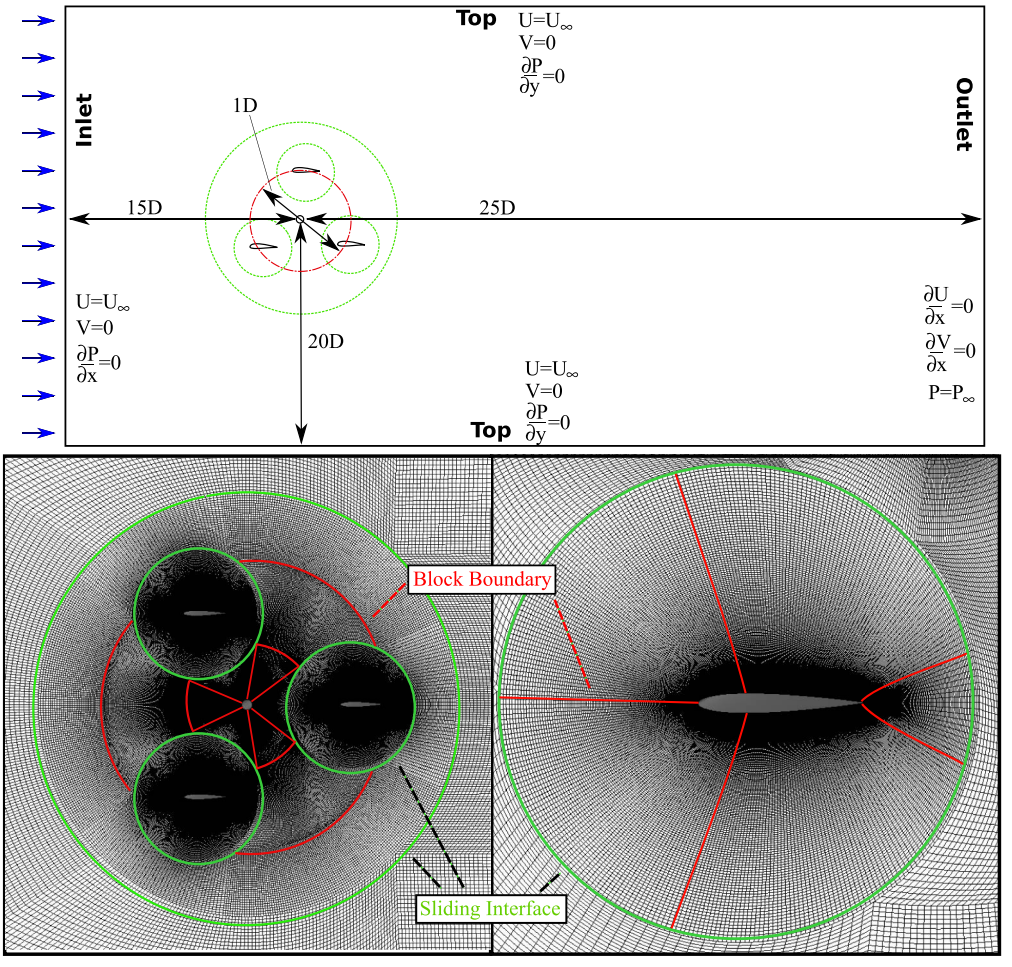

Fig. 6 Snapshots of the grid for CFD simulation. Structured cell blocks are divided with red lines, wall boundaries are shown in black, and cyclic AMI boundary conditions are in green.

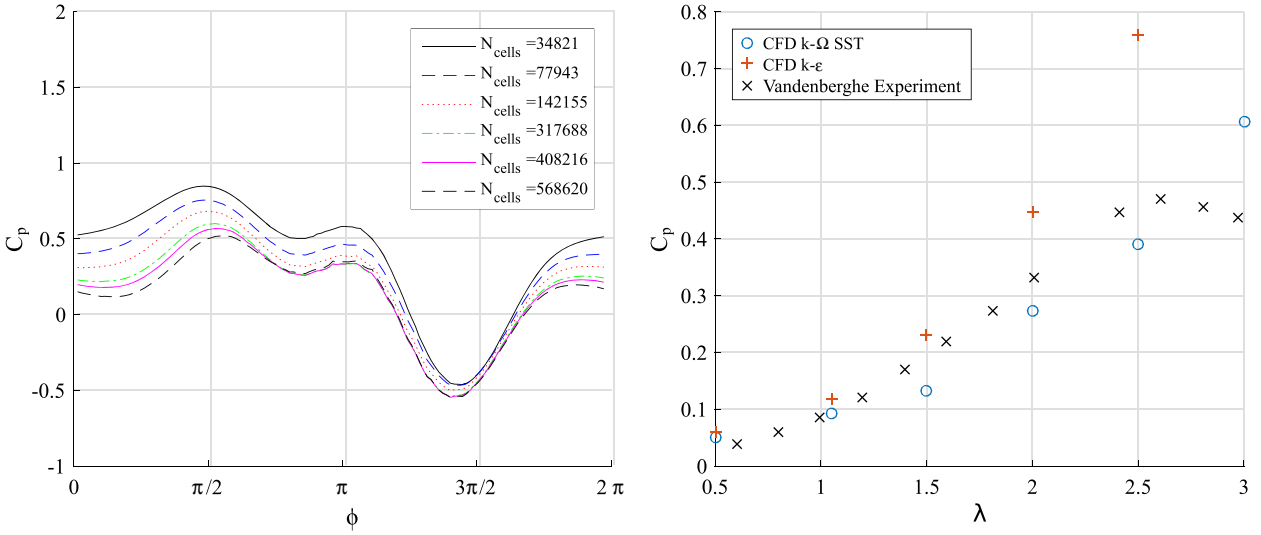

Fig. 7 Cyclic coefficient of power for one blade for a series of grids in a mesh refinement study (left), and selected grid compared with experimental data from the Vandenberghe and Dick experimental cycloturbine (right) [12,18]. No error analysis was provided on historical experimental data.

experiment. Although the k–ϵ model overestimates the performance and the k–Ω SST model generally underestimates the result, the k–Ω SST routine better predicts the trend and was used in the present study. Both turbulence models substantially overestimate the performance of the turbine at TSRs over 3 and fail to capture the downward trend. Vandenberghe and Dick do not explain this downward trend, but it likely results from the increase in turbine parasite power at high rotational speeds. Because the 2-D simulation does not compute the support structure drag, it could not model such a detriment to performance. Regardless, the simplified 2-D RANS simulation does not accurately match the experimental data. Consequently, the simulation is only used for qualitative comparison between pitching motions.

V. Determination of Optimal Blade-Pitch Kinematics

A multistep mathematical process translates optimal flow conditions into attainable pitch motions. First, Sec. V.A derives the computation of blade lift and drag characteristics in terms of the optimal inflow factors. Section V.B proposes a novel semi-empirical curvilinear flow blade lift and drag coefficient model, which forecasts the blade angles of attack needed to produce the ideal blade lift coefficients. In many cases, finite blade lift coefficients cannot attain the optimal flow conditions predicted by flux-line theory. This is examined in Sec. V.C, which develops dual-deceleration schemes that extract more power by attainable, but nonoptimal, flow conditions. These elements are synthesized to determine the actual experimental cam shapes in Sec. V.D.

A. Determine $C_l(s)$

As detailed in [16], flux-line pure momentum theory determines the ideal inflow factor functions $a_u(s)$ and $a_d(s)$ that achieve the highest coefficient of performance. For implementation, these factors must be related to blade angle of attack and then blade pitch. An intermediate step is to identify the required blade lift and drag coefficients. By definition in flux-line theory, only the force parallel to the streamline produces a deceleration of the flow; thus,

$$f_{\|u}(s) = \frac{1}{2}\rho V_{r_u}^2 \sigma[C_{d_u}(\alpha_u)\cos\zeta_u - C_{l_u}(\alpha_u)\sin\zeta_u]$$
$$= \frac{1}{2}\rho V_{r_u}^2 \sigma\left[C_{l_u}\frac{D}{L}(\alpha_u)\cos\zeta_u - C_{l_u}(\alpha_u)\sin\zeta_u\right] \quad (5)$$

Rearranging yields

$$C_{l_u} = \frac{f_{\|u}(s)}{(1/2)\rho V_{r_u}^2 \sigma[(d/l)\cos\zeta_u - \sin\zeta_u]} \quad (6)$$

where

$$V_{ru}^2 = (\Omega r\cos\gamma_u + V_\infty(1-a_u))^2 + (\Omega r\sin\gamma_u)^2 \quad (7)$$

Expansion provides a more useful form of the relative velocity

$$V_{ru}^2 = \Omega^2 r^2\left[1 + \frac{2(1-a_u)}{\lambda}\cos\gamma_u + \frac{(1-a_u)^2}{\lambda^2}\right] \quad (8)$$

Substituting Eq. (8) into Eq. (6) yields

$$C_{l_u} = \frac{f_{\|u}(s)}{(1/2)\rho\Omega^2 r^2[1 + (2(1-a_u)/\lambda)\cos\gamma_u + ((1-a_u)^2/\lambda^2)]\sigma[(D/L)\cos\zeta_u - \sin\zeta_u]} \quad (9)$$

Note that

$$f_{\|u} = (V_\infty - V_{uw})\frac{1}{2}\rho V_u \sin\gamma_u = V_\infty^2(1-a_u)a_u\rho\sin\gamma_u \quad (10)$$

Substituting provides

$$C_{l_u} = \frac{V_\infty^2(1-a_u)a_u\rho\sin\gamma_u}{(1/2)\rho\Omega^2 r^2[1 + (2(1-a_u)/\lambda)\cos\gamma_u + ((1-a_u)^2/\lambda^2)]\sigma[(D/L)\cos\zeta_u - \sin\zeta_u]} \quad (11)$$

which simplifies to

$$C_{l_u} = \frac{2(1-a_u)a_u \sin\gamma_u}{\sigma[\lambda^2 + 2\lambda(1-a_u)\cos\gamma_u + (1-a_u)^2][(D/L)\cos\zeta_u - \sin\zeta_u]} \tag{12}$$

where

$$\zeta_u = \arctan\left(\frac{\lambda \sin\gamma_u}{\lambda\cos\gamma_u + (1-a_u)}\right) \tag{13}$$

The same procedure is applied to the downstream flux line and yields

$$C_{l_d} = \frac{4\sin\gamma_d(1-2a_u)^2(1-a_d)a_d}{[\lambda^2 + 2\lambda\cos\gamma_d(1-2a_u)(1-a_d) + (1-2a_u)^2(1-a_d)^2]\sigma[(D/L)\cos\zeta_d + \sin\zeta_d]} \tag{14}$$

Flux-line pure momentum theory identified that, for optimum turbine-only flow, $a_u(s) = 0$; thus,

$$C_{l_d} = \frac{4\sin\gamma_d(1-a_d)a_d}{[\lambda^2 + 2\lambda\cos\gamma_d(1-a_d) + (1-a_d)^2]\sigma[(D/L)\cos\zeta_d + \sin\zeta_d]} \tag{15}$$

Note that

$$\zeta_d = \arctan\left(\frac{\lambda \sin\gamma_d}{\lambda\cos\gamma_d + (1-2a_u)(1-a_d)}\right) \tag{16}$$

Figure 8 plots Eq. (15) over a range of TSRs. An analysis in Sec. V.B shows that the maximum possible lift coefficient for symmetric blades in curvilinear flow will likely be less than 0.5. Thus, it will only be possible to achieve optimal lift coefficients with symmetric airfoil sections at high TSRs (greater than 3). Analyzing Eq. (15) leads to several important observations.

1) As TSR increases, the required downstream lift coefficient approaches zero. This is sensible because high TSRs imply high relative blade velocities. These high relative velocities only require small lift coefficients to generate sufficient deceleration forces. The opposite is also true. As the TSR decreases toward zero, the term $\sin\zeta_d$ approaches zero, and large downstream lift coefficients are required to generate the same decelerating forces.

2) As the rotor solidity increases, the required downstream lift coefficient decreases for a given TSR. Larger blades need smaller lift coefficients to decelerate the flow equivalently. Alternatively, for a given maximum blade lift coefficient, larger blades can achieve the same flow deceleration at a lower TSR.

3) Regardless of TSR, near the top and bottom of the flux lines ($s \to 0$ and $s \to 1$), the streamlines lie tangent to the rotor disk ($\gamma_d \to 0$ and $\gamma_d \to \pi$), and aerodynamic forces cannot be generated ($C_{l_d} \to \infty$) at the correct angle, effectively decelerating the flow. Healy [11] previously noted this.

4) Drag may decrease the lift coefficient required to produce a given deceleration of the flow. However, this does not imply that it will increase power production. Drag will reduce net power production at all rotor locations when the TSR is greater than 1 and the portions where the blade proceeds into the flow at lower TSRs. It is possible that pitch motions that maximize drag on the retreating blades when the TSR is less than 1 could increase flow deceleration and increase power production.

B. Prestall Blade-Element Model in Curvilinear Flow

To design blade-pitch kinematics, the lift coefficient must be related to the blade angle of attack. This connection is straightforward in steady rectilinear flow. However, few models are available for the curvilinear, centrifugally loaded, unsteady flowfield within cycloturbines. Ideally, fundamental research will identify the relevant flow physics in this environment and develop a comprehensive and accurate blade-element method. In the absence of such work, a simple semi-empirical model is proposed for initial experimentation with consideration of the state of the art.

Several authors [24–26] incorporated unsteady airfoil models into their blade-element methods for VAWTs and cyclorotors. However, these models are based on rectilinear flow studies, and their accuracy for the curvilinear flow environment of moderate and high chord-to-radius ratio turbines is questionable. Regardless, the discrepancy between unsteady and steady models depends mainly on the reduced

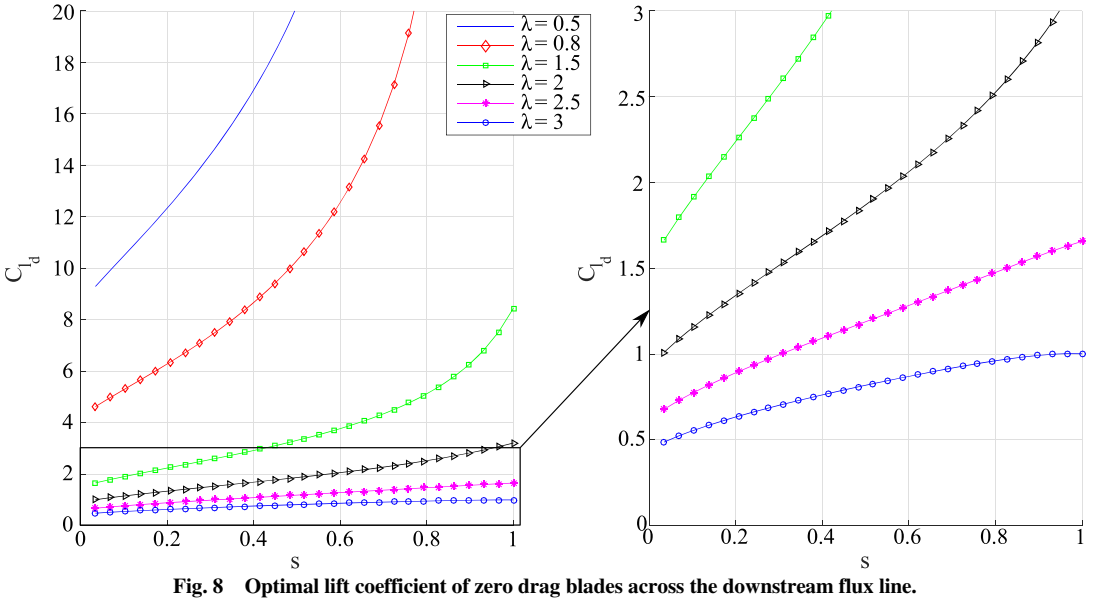

Fig. 8 Optimal lift coefficient of zero drag blades across the downstream flux line.

frequency [27]. This study chose to omit unsteady effects because the reduced frequency using the mean blade relative velocity,

$$k = \frac{c}{2r}\frac{\partial\alpha}{\partial\phi}\frac{\lambda}{\sqrt{1+\lambda^2}}$$

is generally less than 0.05 for the present turbine geometry. Centrifugal effects on the boundary layer are also neglected in absence of fundamental research.

Curvilinear flow will substantially alter the aerodynamic coefficients and must be considered. Migliore et al. [9] and Akimoto et al. [28] proposed polar and complex coordinate mappings to translate the physical airfoil shape in curvilinear flow into a representation in rectilinear flow, which can be analyzed with traditional methods. Although coordinate mapping is the most reliable model available, it is cumbersome to mathematically implement in a pitching optimization method. A given airfoil section has a separate transformed rectilinear airfoil shape for every blade-pitch angle at each cyclic position, which depends on the nature of the turbine flowfield. After transformation, computation of the aerodynamic characteristics of the blade is nontrivial.

Instead, a simple semi-empirical curvilinear-flow blade aerodynamics model for preliminary pitching motion design is proposed. Future studies in this area should be used to validate, improve, or replace this model. It is assumed that a linear relationship exists between lift and angle of attack up to stall and that a quadratic relationship exists for drag similar to rectilinear flow. These relationships are corrected for curvilinear flow by the inclusion of correction coefficients ($\Delta C_{L_{vc}}$ for virtual camber, $\Delta\alpha_{vi}$ for virtual incidence, and $\Delta C_{D_{cf}}$ for the change in drag coefficient from curvilinear flow) and an effectiveness parameter ψ. Mathematically,

$$C_L = C_{L_o} + \psi\Delta C_{L_{vc}} + (\alpha + \psi\Delta\alpha_{vi})C_{L_\alpha} \tag{17}$$

and

$$C_D = C_{D_o} + \psi\Delta C_{D_{cf}} + \frac{C_L^2}{e\pi\mathcal{R}} \tag{18}$$

where e is the Oswald efficiency factor, and

$$\mathcal{R} = \frac{b}{c} = \frac{nb}{2r\sigma\pi}$$

is the blade aspect ratio. It is further assumed that the correction coefficients are constant throughout the revolution regardless of blade orientation, but the effectiveness parameter ψ changes from zero to 1 as the TSR increases from zero to infinity. The curvilinear effect quickly becomes significant as the TSR increases above 1, but the flow is more nearly rectilinear at TSRs less than 1. Thus, we define the effectiveness parameter as

$$\psi = \frac{\lambda^2}{1+\lambda^2} \tag{19}$$

The three correction coefficients can be determined experimentally. Using the experiment described in Sec. III, we performed a series of tests by fixing all three blades at a constant pitch, rotating the turbine in a zero-wind condition, and measuring the torque. It can be assumed that there is no significant induced flow through the blades because the turbine is a high aspect ratio, and the spoke structure partially blocks flow through the top and bottom of the turbine. In the absence of induced flow, the angle of attack of the blades is equivalent to the blade pitch. The blade coefficient of drag is determined by postprocessing of the recorded torque, rotational speed, and air density. Figure 9 plots the blade coefficient of drag of the turbine for varying blade pitch.

The experimentally determined empirical coefficients are summarized in Table 2, which enable Eqs. (17) and (18) to fully describe the prestall lift and drag characteristics of the blades at a range of TSRs, as shown in Fig. 10. The lift curve shifts down and to the right as the range of TSR increases, whereas the drag coefficient shifts up and to the right. This method has important implications for the realization of flux-line optimal pitching kinematics and model limitations.

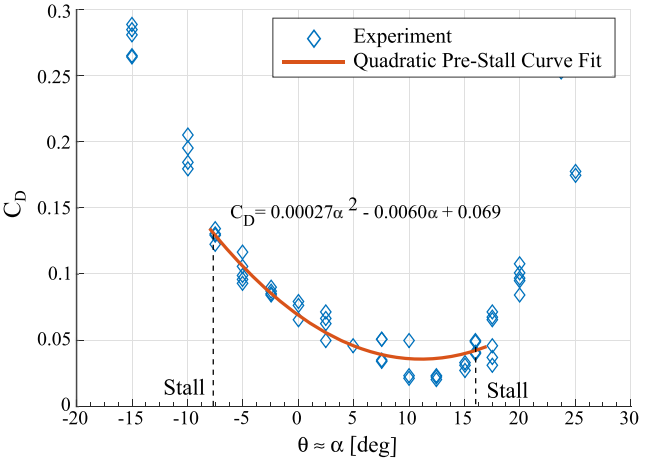

Fig. 9 Experimentally determined blade drag coefficient alongside quadratic regression curve of prestall data.

1) Curvilinear flow substantially alters blade forces, and designing highly efficient cycloturbines and cyclorotors requires a deeper-than-available understanding of curvilinear, unsteady blade aerodynamics.

2) Flux-line theory concludes that the downstream flux line should decelerate the flow for maximum power. However, curvilinear flow effects decrease the capability of the turbine to achieve this deceleration in the rear and increases the ability across the upstream flux line. This further exacerbates the required departure from fixed-pitch and traditional pitch motions for symmetric blades and suggests that changing the blade airfoil section could substantially increase turbine power. The blades will have to be specifically designed to counter curvilinear flow effects. This might be accomplished by an inverse conformal transformation as described by Migliore et al. [9] or a more-advanced computational optimization method. The NACA 0012 blades in this study can achieve only low lift coefficients and must operate just below stall on the downstream flux line under low and moderate TSRs.

3) The small downstream maximum lift coefficient denies operation of symmetric-airfoil cycloturbines in a combined propeller–turbine operating mode at reasonable TSRs. Under those conditions, the downstream blades cannot adequately decelerate the speed of the freestream wind, much less a high-velocity wake produced by upstream blades acting as a propeller. High TSRs and purpose-designed airfoil sections could be investigated for operation in a combined propeller–turbine operating mode, but there would be increasing structural support drag. Overall, the outlook for this strategy is dismal.

4) Numerous existing empirical and semi-empirical relationships provide a convenient sanity check for the experimentally determined coefficients. Adjusting the lift slope expression by Bouton [29] to include an Oswald efficiency factor suggests a rectilinear blade lift slope value of 0.0691 /deg. This is within 15% (relative uncertainty) of the experimentally determined value.

5) Because even this high-solidity cycloturbine cannot sufficiently decelerate the flow through the downstream flux line for maximum performance, it is worth exploring alternative deceleration schemes.

Table 2 Geometry and coefficients

Category	Value
Assumed rectilinear drag coefficient C_{D_o}	0.02
Lift slope C_{L_α}	3.371 /rad (0.059 /deg)
Virtual incidence coefficient $\Delta\alpha_{vi}$	−0.0742 rad (−4.25 deg)
Virtual camber coefficient $\Delta C_{L_{vc}}$	−0.402
Virtual drag coefficient $\Delta C_{D_{cf}}$	0.0156

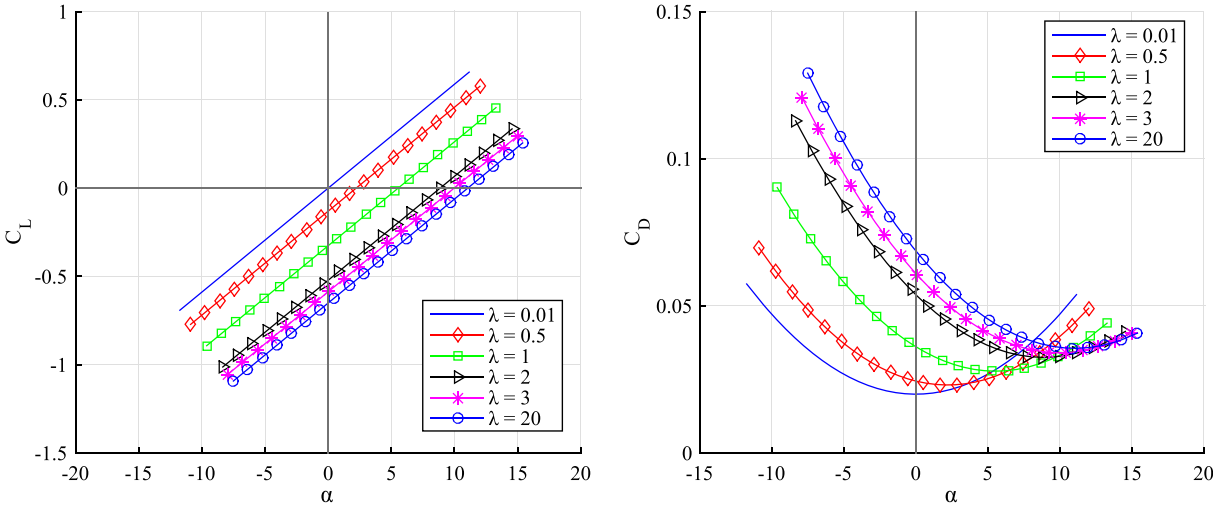

Fig. 10 Lift and drag curves for various TSRs implementing the corrected curvilinear model with experimentally determined coefficients.

These decelerate the flow over the upper and lower flux line to compensate for the inability to fully decelerate the flow exclusively in the rear half.

C. Dual-Deceleration Optimal Inflow Schemes

Although optimal theoretical cycloturbine flow deceleration occurs only across the downstream flux line, realistic cycloturbines cannot usually attain this condition. In these systems, the blade is unable to adequately slow the fluid for the optimal turbine power coefficient, except at prohibitively high TSRs, due to the small downstream maximum blade lift coefficient. Instead, flow deceleration and blade pitch must be optimized as a constrained problem: "what are the optimal cycloturbine flow deceleration functions, given real blade lift-drag characteristics?"

For a basic understanding of the flow physics, consider fixing the inflow coefficient functions $a_u(s)$ and $a_d(s)$ as constants (A_u and A_d) as previously described [16]. Under these circumstances, the power coefficient is

$$C_p = \frac{4\pi}{\int_0^1 (\mathrm{d}s/\sin\gamma_u)} \frac{A_u(1-A_u)+(1-2A_u)^2 A_d(1-A_d)}{1/(1-A_u)+\kappa/(1-2A_u)(1-A_d)} \tag{20}$$

where

$$\kappa = \frac{\int_0^1 (\mathrm{d}s/\sin\gamma_d)}{\int_0^1 (\mathrm{d}s/\sin\gamma_u)} \tag{21}$$

is a measure of the angular distribution of the flow through the rotor, which for a cycloturbine will be slightly less than 1. Figure 11 plots C_p for varying values of A_u and A_d. Positive values denote a deceleration of the flow, and negative values denote an acceleration. Within this simplified system, the preceding optimization question simplifies to: "If a cycloturbine can attain only a certain downstream inflow factor A_d, then what is the optimal upstream inflow factor A_u?"

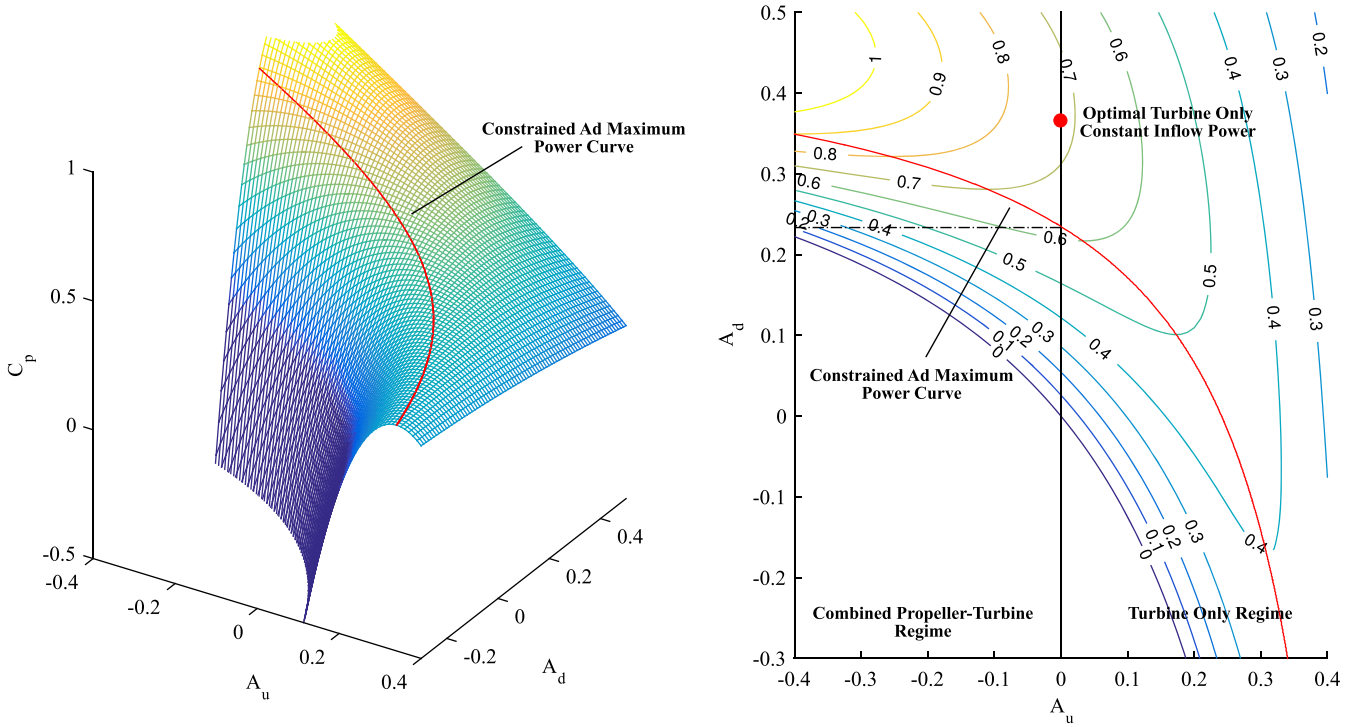

Fig. 11 Variation of coefficient of power for a constant inflow distribution over the upstream and downstream flux lines [$a_u(s) = A_u$ and $a_d(s) = A_d$] with $\int_0^1 (\mathrm{d}s/\sin\gamma_u) = \pi/2$ and $\kappa = 1$. The mesh surface (left) and contour plot (right) are colored according to the distribution of C_p.

This optimum is determined for a particular angular distribution κ:

$$\int_0^1 \frac{\mathrm{d}s}{\sin\gamma_u}$$

by solving when $\partial C_p/\partial A_u = 0$ for a particular value of A_d. The red line in Fig. 11 plots this solution, which follows slightly beneath the ridge of the surface. If $0 < A_d < 0.241$, a greater C_p is possible by using the upstream blades for power extraction ($A_u > 0$). Intuitively, the upstream blades should decelerate the flow more when the downstream blades cannot decelerate the flow as much. If the downstream flux line can attain $A_d > 0.241$, the maximum C_p occurs in a combined propeller–turbine operating mode, and the upstream flux line should add momentum to the flow ($A_u < 0$). However, assuming that higher-order inefficiencies make this operating mode unfeasible, the maximum C_p will continue to build with increasing A_d and $A_u = 0$ until the optimal turbine-only constant inflow power coefficient point is reached ($A_u = 0$, $A_d \approx 0.39$), which is marked by a red dot in Fig. 11. Because the symmetric airfoils adopted in the present experiment can only achieve low lift coefficients during the downstream portion of their revolution, blade-pitch motions that use a dual-deceleration inflow scheme were selected for this effort.

D. Determination of Experimental Blade-Pitch Kinematics and Cam Shapes

In this study, optimal blade-pitch kinematics were determined by numerically optimizing the inflow factor functions $a_u(s)$ and $a_d(s)$, as outlined in [16], under the additional constraint that the maximum blade lift coefficient cannot exceed the maximum specified by Fig. 10. This optimization used a constrained sequential nonlinear optimization algorithm using the Matlab function fmincon, in conjunction with the semi-empirical blade lift coefficient model in Sec. V.B. Figure 12 shows the optimal inflow functions for the experimentally evaluated TSRs. The upstream inflow factor is a positive function for all cases, which compensates for a suboptimal downstream inflow coefficient along the same streamline. All of the TSRs greater than 1 have inflow factors along the upstream flux line that swell with increasing streamline coordinate, which corresponds to a decreasing inflow coefficient along the downstream flux line. Increasing the TSR reduces the dependence of the rotor on the upstream flux line for flow deceleration.

The optimal lift coefficients are determined from these inflow distributions via Eqs. (12) and (14) and translated into the required blade angle of attack via Eq. (17). Figure 13 plots angle of attack and lift coefficient as a function of cyclic blade position for the experimentally tested TSRs. The linear relationship between the angle of attack and lift coefficient is manifested in the two similarly shaped plots, but the relative magnitude of the functions change with TSR. At $\lambda = 0.5$ the curvilinear flow effectiveness parameter is small, and the blades can achieve a higher lift coefficient in the rear half of the revolution at a lower absolute angle of attack. Moreover, at this low TSR, it is most efficient to maximize the angle of attack (and hence lift coefficient and flow deceleration) in both the upstream and downstream portions of the turbine. As the TSR increases, the turbine achieves a lower maximum lift coefficient across the downstream flux line. Because the relative blade velocity (and correspondingly the blade force) increases, the blades decelerate the flow more effectively across the downstream flux line. This higher deceleration requires smaller deceleration across the upstream flux line and results

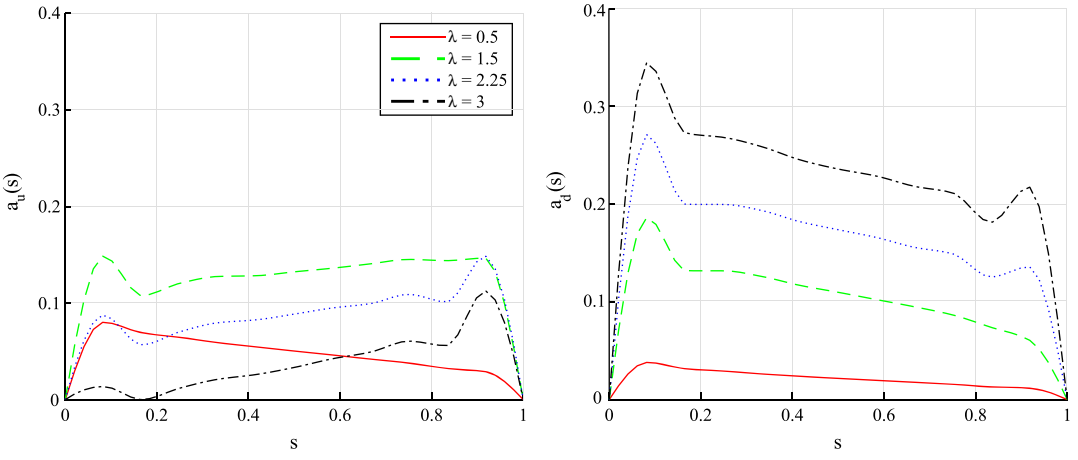

Fig. 12 Upstream (left) and downstream (right) inflow factor functions for the three experimentally selected TSRs.

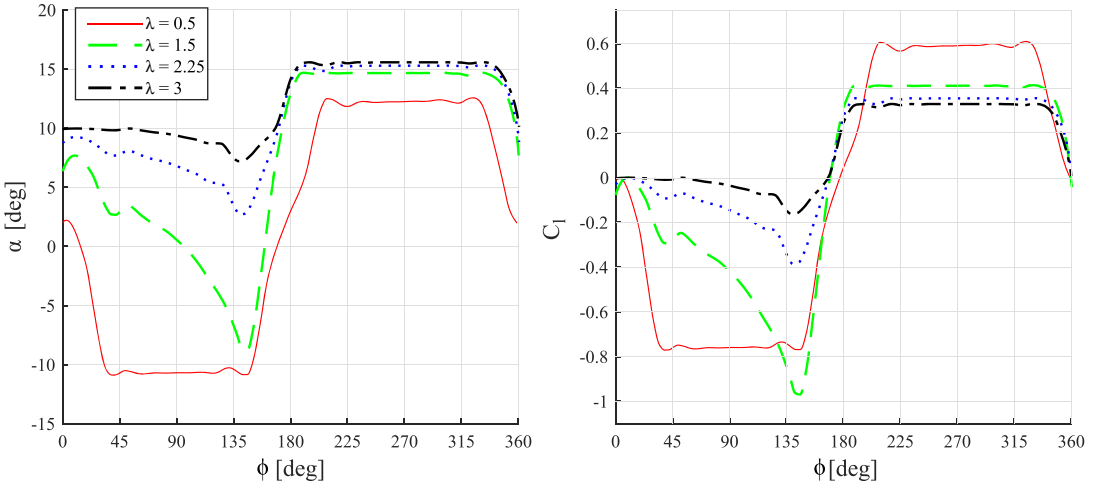

Fig. 13 Numerically optimized angle of attack (left) and corresponding lift coefficient (right) for the three experimentally selected TSRs.

in smaller negative blade angles of attack in the front half of the revolution.

Also, note from Fig. 13 that, as the TSR increases, the portion of the revolution that the blades remain at a positive and negative angle of attack increases and decreases, respectively. This corresponds to the increasing expansion of flow through the turbine, which reduces the portion of the rotor spanned by the upstream flux line and stretches the downstream flux line. Although the expansion of the flow is not directly mathematically tied to the TSR, an increasing TSR magnifies the capability of the blades to decelerate. The small bumps shown in Fig. 13 are likely a result of numerical optimization. To ensure reliable, smooth operation, these deviations were mathematically smoothed by specifying a maximum blade-pitch rotational acceleration when the optimal pitch was computed.

These optimal angles of attack are translated into blade pitch by incorporating the flow angles determined by flux-line theory through the expressions

$$\theta_u(s) = \alpha_u(s) + \gamma_u(s) - \zeta_u(s) \tag{22}$$

and

$$\theta_d(s) = \alpha_d(s) - \gamma_d(s) + \zeta_d(s) \tag{23}$$

These blade-pitch functions are translated from dependence on streamline coordinate s to polar coordinates ϕ by substitution of the flux-line theory determined functions $\phi_u(s)$ and $\phi_d(s)$. After this transformation, blade pitch is directly related to the position of the blades around the rotor [i.e., the original objective function $\theta(\phi, \lambda, \sigma)$]. These pitch motions are then related to a cam shape to actuate them. Figure 14 plots the optimal functions and cam shapes for the four experimentally selected TSRs.

VI. Experimental Power Measurement

Flux-line optimal blade-pitch motions increased power production at the design TSRs when compared to sinusoidal blade pitching and fixed-pitch turbines. Figure 15 compares the gross power coefficient (power from blades alone) of the experimental turbine implementing different blade-pitch motions as well as other high-performance cycloturbines. The flux-line optimal pitching motions produced 68 and 73% more power than the fixed-pitch motion at two design conditions $\lambda = 1.5$ and $\lambda = 2.25$, respectfully.

Although this experiment implemented different two-dimensional cams to evaluate individual TSR values, a three-dimensional cam (or other mechanism) could optimize power at every TSR [30]. The "possible on-design curve" in Fig. 15 supposes that the cam shape is optimally adapted to TSR. At off-design conditions, the best flux-line

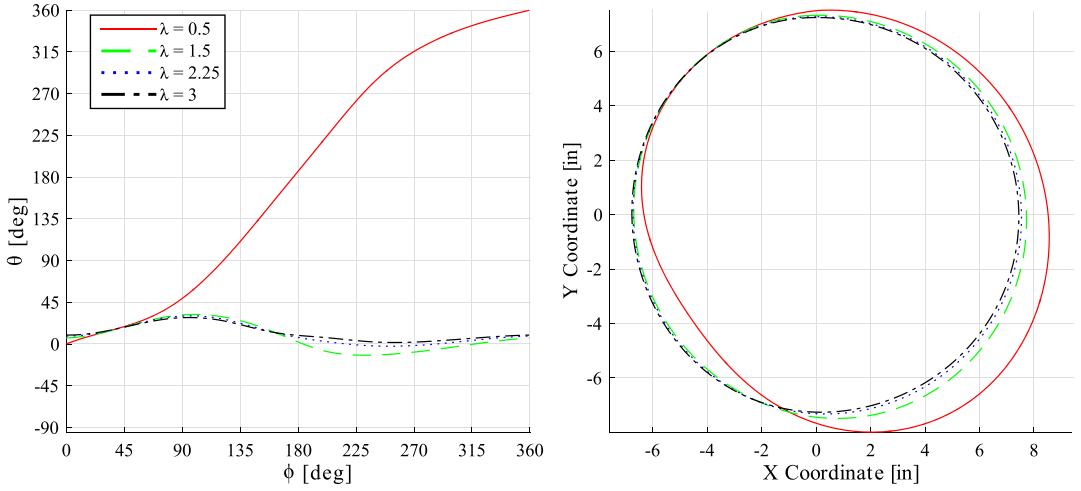

Fig. 14 Optimal blade-pitch kinematics identified by flux-line theory for the fours experimentally sleeted TSRs (left), and corresponding cam profiles (right).

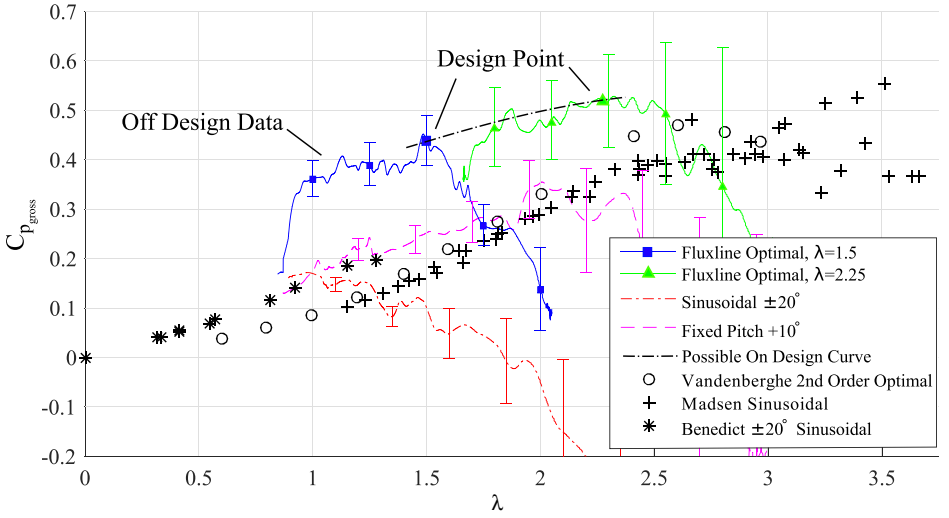

Fig. 15 Experimental gross power (blades alone) and comparison with various cycloturbine experiments [3,12,17,18]. Error bars represent a 95% confidence interval for the true mean experimental power coefficient accounting for both systematic and precision errors.

optimal pitching motion performed substantially better than the fixed-pitch and sinusoidal pitching motions. Consequently, a low-cost commercial application might use a single two-dimensional cam rather than implement a more complicated three-dimensional cam required to optimize the pitching kinematics for every TSR. These high-efficiency pitch motions made this experimental turbine the most efficient low TSR VAWT to date. The listed cycloturbine experiments from Vandenberghe and Dick [12,18], Madsen and Lundgren [17], and Benedict et al. [3] are among the most efficient VAWTs reported in the literature. Fixed-pitch Darriues (lift) type VAWTs usually do not exceed a power coefficient greater than 0.4, and then only at TSRs greater than 5. Savonius (drag) type VAWTs are much less efficient and generally not greater than 0.15 [31].

The capability to produce power at low TSRs is of particular importance for VAWTs, which usually require a rotating support structure. This structure causes drag during rotation, which reduces the net power produced by the turbine. This drag disproportionately punishes high-rotational-speed turbines because the lost power increases with the cube of the rotational velocity. At a fixed wind velocity, higher TSRs correspond to higher rotational speeds that attenuate the power collected for a given gross aerodynamic power coefficient. Figure 16 compares the net power coefficient output to the generator from the present experiments and those reported by Vandenberghe and Dick [12] and Madsen and Lundgren [17]. The flux-line optimal (design condition $\lambda = 1.5$) pitching motion achieved a higher net power coefficient than any other published cycloturbine results. Operating at low rotational speeds also reduces the structural loads and fatigue cycles on the components of the system and provides a high starting torque for water pumping, heat pumping, desalination, or other mechanical applications. However,

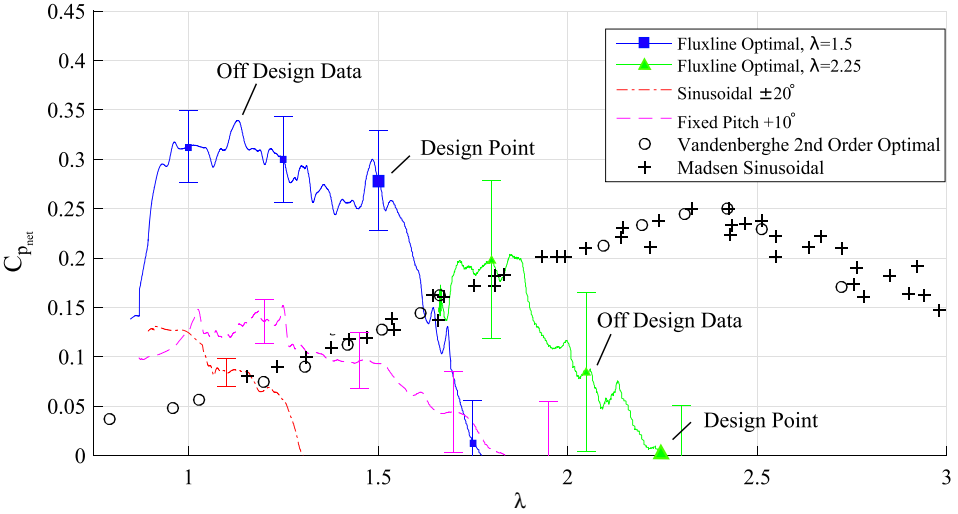

Fig. 16 Comparison of net power (shaft power to generator) of experimental pitching motions with Madsen and Lundgren [17]. Error bars represent a 95% confidence interval for the true mean experimental power coefficient accounting for both systematic and precision errors.

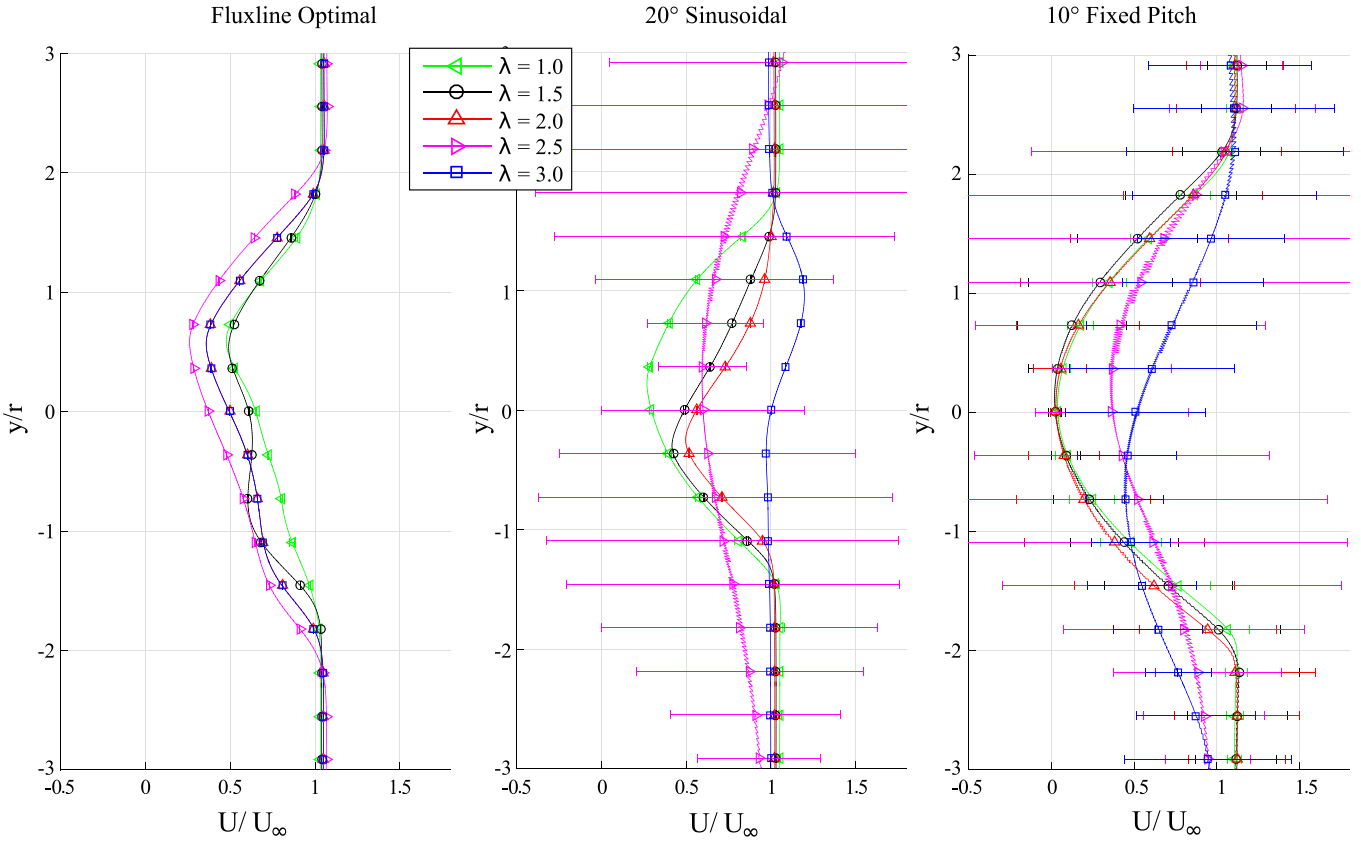

Fig. 17 Comparison of $x = 10r$ wake structure for various pitching motions. Error bars provide the rms value.

operating in this regime for electrical power production will require a higher torque generator or larger mechanical gear ratio.

A couple of operational characteristics of the turbine are worth noting. The only noticeable noise was from the cam bearings crossing irregularities in the cam track. A lack of aerodynamic noise suggests that cycloturbines are aerodynamically quiet. During data collection, the turbine rotational speed was maintained by a motor–generator. However, once electric power was disconnected, the turbine would initiate rotation from a static condition in even light wind conditions for the flux-line optimal and sinusoidal pitch motions. Even pitch kinematics optimized for a single TSR will be self-starting.

VII. Wake Structure Predicted by Computational Fluid Dynamics

CFD captures qualitative flow details beyond the capacity of experiments and explains the enhanced performance of flux-line optimal blade-pitch kinematics. The wake characteristics are especially important to wind turbines because its velocity magnitude indicates the amount of energy extracted by the turbine and whether it does so in an ordered or chaotic manner. Figure 17 plots the mean velocity of the wake at a downstream location of five turbine diameters, where error bars denote the corresponding rms of the velocity. Large rms values are correlated with substantial turbulent fluctuations in velocity, whereas negligible rms values indicate steady flow.

Flux-line optimal pitch motions yield a steady wake with even flow deceleration from the top to the bottom of the turbine at all TSRs. The deceleration in the top portion ($y/r > 0$) approaches the ideal value of one-third the freestream value. The top portion of the turbine retards the flow slightly more than the bottom, which correlates with higher blade velocities and larger prestall forces. Figure 18 compares snapshots of the streamwise velocity for $\lambda = 1.5$. Although blade passage causes initial unsteadiness immediately behind the turbine, the flow quickly reaches the steady uniform wake observed in Fig. 17.

In stark contrast, the sinusoidal pitching motion wake pattern changes substantially with TSR from a significant deceleration at low TSRs to acceleration (cyclorotor operation) at high TSRs. As the rotation rate of the turbine increases, the blade angle of attack proceeds toward zero and then reverses sign. The steadiness of the wake also varies with TSR. At $\lambda = 1$ and $\lambda = 1.5$, the flow is steady,

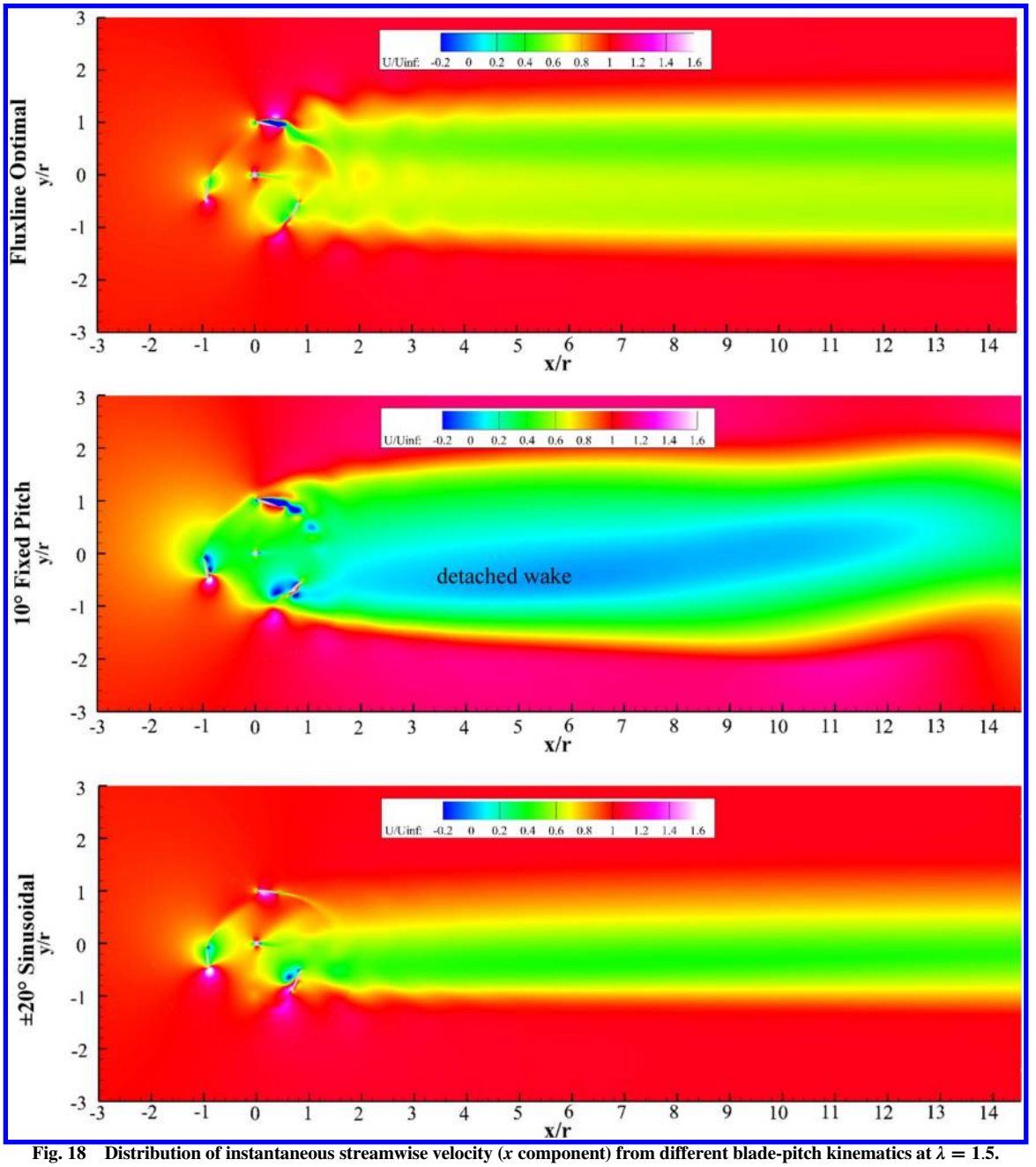

Fig. 18 Distribution of instantaneous streamwise velocity (x component) from different blade-pitch kinematics at $\lambda = 1.5$.

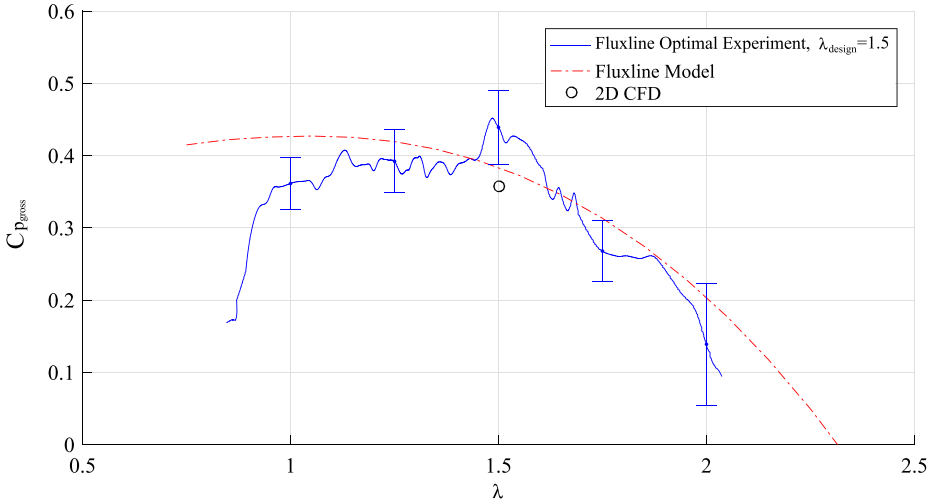

Fig. 19 Comparison of flux-line theory prediction, experimental data, and CFD for the flux-line optimal $\lambda = 1.5$ pitching motion. Flux-line theory implements the simplified semi-empirical blade-element method described in Sec. V.B. Error bars on experimental results indicate the 95% confidence interval for the true mean experimental power coefficient accounting for both systematic and precision errors.

but turbulence increases with TSR until the turbine begins acting as a cyclorotor, where the unsteadiness again disappears. The ±20 deg sinusoidal pitching motion produces the greatest power with the TSR slightly less than 1.5, as shown in Fig. 18 (middle panel). The wake quickly becomes steady at a value near the optimal deceleration ($U_{\text{wake}}/U_\infty \approx 1/3$), but does so in an uneven manner. A substantial quantity of energy remains unharnessed in the top portion of the turbine (there, $U_{\text{wake}}/U_\infty > 1/3$).

The 10 deg fixed-pitch motion wake produces a turbulent wake at all TSRs, but the magnitude of the deceleration varies. At low TSRs, the flow is uniformly detached from the turbine and forms a velocity distribution similar to that behind a blunt object. At those TSRs, the turbulence is greatest near the maximum velocity shear. Presumably, this invariance with TSR is due to fully stalled blades over most of the revolution. As shown in Fig. 18 (bottom panel) for $\lambda = 1.5$, the flow behind the turbine is completely detached, and the blockage of the wind causes an increase in fluid velocity outside the wake. As the TSR increases, the wake velocity increases, and the turbulence is uniformly distributed.

VIII. Comparison of Flux-Line Prediction, Experimental Data, and Computational Fluid Dynamics

The experiment in this study provided an opportunity to evaluate the predictive capability of flux-line theory and 2-D CFD. Figure 19 compares the experimental data for the flux-line optimal $\lambda = 1.5$ pitching motion to a flux line and 2-D CFD prediction. In this instance, the semi-empirical blade-element model from Sec. V.B was implemented to predict blade forces from the angle of attack and flow velocities. At the design TSR of 1.5, the CFD and flux line models underpredict the mean experimental power by 18 and 13% relative error, respectively. Flux-line theory predicts the performance of the turbine within experimental error for TSRs above 1.25. At TSRs near unity, the blades will experience extreme angles of attack and likely stall with this pitch motion. The semi-empirical blade-element model implemented in this study does not model blade stall and should not be expected to model this regime accurately. Future work should improve this blade-element model for poststall conditions.

IX. Conclusions

Optimal blade pitch for cycloturbines is predicted via an inverse method that computes blade pitch from the optimal flow deceleration functions determined by flux-line theory [16]. This inverse method uses a semi-empirical curvilinear flow aerodynamic coefficient model to compute blade angle of attack from the required blade forces. These optimal blade-pitching kinematics were compared with traditional fixed-pitch and sinusoidal blade-pitch kinematics on a series of truck-mounted cycloturbine tests and through a 2-D RANS simulation. The following conclusions are drawn from this study.

1) Proper design of vertical-axis wind-turbine blade-pitching motions substantially increases the power that they can extract from the wind. Specifying the proper pitch function is equally influential as other key design features including rotor solidity, blade geometry, and operating TSR.

2) Curvilinear flow decreases the maximum coefficient of lift over the downstream flux line and increases the absolute value (negative) on the upstream flux line. This prevents turbine blades from achieving maximum power by decelerating the flow only over the downstream flux line except at high TSRs. Instead, a real turbine can achieve higher power coefficients at low TSRs by extracting power throughout the blade revolution. As the TSR increases, the blades can extract more energy along the downstream flux line and less along the upstream flux line to increase wind energy extraction.

3) Flux-line optimal blade-pitching motions achieve a higher gross power coefficient than fixed-pitch or sinusoidal blade-pitch motions and do so over a wider range of TSRs. Significantly, this includes low TSRs where cycloturbines produce higher net power due to lower parasite drag and mechanical losses. This performance improvement was demonstrated experimentally and computationally. At the design TSR of 1.5, the experimental turbine achieved a mean gross power coefficient of 0.44, with a 95% confidence interval for the true mean power coefficient ranging from 0.39 to 0.49. At the design TSR of 2.25, the turbine achieved a mean gross power coefficient of 0.52 with the 95% confidence interval for the true mean power coefficient spanning 0.43 to 0.61. At the design TSR of 1.5 and 2.25, the optimal blade-pitch kinematics achieved approximately 120 and 30% higher power coefficients, respectively, than experiments by Vandenberghe and Dick [12].

4) CFD simulations show that flux-line optimal blade-pitching kinematics achieve a higher coefficient of power by evenly extracting energy from the flow such that the velocity of the wake approaches the ideal one-third freestream value. They can achieve this deceleration across a wide range of TSRs. This contrasts efficient sinusoidal motions, which only decelerate the flow over a narrow range of TSRs and do so unevenly. Even the best fixed-pitch turbines chaotically brake the flow, causing extensive flow detachment behind the turbine.

5) Flux-line theory implementing a simple semi-empirical blade-element model forecast experimental turbine power within the experimental error for a broad range of TSRs. At the design TSR, this variation of flux-line theory underpredicted the mean experimental power by 13%, and the 2-D RANS simulation underpredicted the power by 18% relative error.

Future studies should build a fundamental understanding of curvilinear flow aerodynamics and develop a model to predict lift, drag, and moment coefficients. Implementing such a model within

the method presented in this paper will improve performance by more accurately realizing the optimal flow deceleration. Other studies should understand the three-dimensional flow through cycloturbines.

Acknowledgments

We thank the U.S. Department of Defense for the National Defense Science and Engineering Fellowship for financial support. Specifically, we thank the U.S. Air Force Research Laboratory for enabling the experimental evaluation of blade-pitching motions through the Summer Faculty Fellowship Program as well as Frederick Schauer and John Hoke for technical guidance.

References

[1] Borg, M., Shires, A., and Collu, M., "Offshore Floating Vertical Axis Wind Turbines, Dynamics Modelling State of the Art. Part 1: Aerodynamics," *Renewable and Sustainable Energy Reviews*, Vol. 39, Aug. 2014, pp. 1214–1225. doi:10.1016/j.rser.2014.07.096

[2] Borg, M., Collu, M., and Kolios, A., "Offshore Floating Vertical Axis Wind Turbines, Dynamics Modelling State of the Art. Part 2: Mooring Line and Structural Dynamics," *Renewable and Sustainable Energy Reviews*, Vol. 39, Nov. 2014, pp. 1226–1234. doi:10.1016/j.rser.2014.07.122

[3] Benedict, M., Lakshminarayan, V., Pino, J., and Chopra, I., "Fundamental Understanding of the Physics of Small-Scale Vertical Axis Wind Turbine with Dynamic Blade Pitching: An Experimental and Computational Approach," *54th AIAA/ASME/ASCE/AHS/ASC Structures, Structural Dynamics, and Materials Conference*, AIAA Paper 2013-1553, 2013. doi:10.2514/6.2013-1553

[4] Dabiri, J., "Potential Order-of-Magnitude Enhancement of Wind Farm Power Density via Counter-Rotating Vertical-Axis Wind Farm Turbine Arrays," *Journal of Renewable and Sustainable Energy*, Vol. 3, No. 4, 2011, Paper 043104. doi:10.1063/1.3608170

[5] Kirke, B. K., "Evaluation of Self-Starting Vertical Axis Wind Turbines for Stand-Alone Applications," Ph.D. Thesis, School of Engineering, Griffith Univ. Gold Coast Campus, Southport, Australia, April 1998.

[6] Sasson, B., and Greenblatt, D., "Effect of Leading-Edge Slot Blowing on a Vertical Axis Wind Turbine," *AIAA Journal*, Vol. 49, No. 9, 2011, pp. 1932–1942. doi:10.2514/1.J050851

[7] Greenblatt, D., Ben-Harav, A., and Mueller-Wahl, H., "Dynamic Stall Control on a Vertical-Axis Wind Turbine Using Plasma Actuators," *AIAA Journal*, Vol. 52, No. 2, 2014, pp. 456–462. doi:10.2514/1.J052776

[8] Parashivoiu, I., Trifu, O., and Saeed, F., "H-Darrieus Wind Turbine with Blade Pitch Control," *International Journal of Rotating Machinery*, Vol. 2009, April 2009, pp. 1–7. doi:10.1155/2009/505343

[9] Migliore, P., Wolfe, W., and Fanucci, J., "Flow Curvature Effects on Darrieus Turbine Blade Aerodynamics," *Journal of Energy*, Vol. 4, No. 2, 1980, pp. 49–55. doi:10.2514/3.62459

[10] Siegel, S., Seidel, J., Cohen, K., and McLaughlin, T., "A Cycloidal Propeller Using Dynamic Lift," *37th AIAA Fluid Dynamics Conference and Exhibit*, AIAA Paper 2007-4232, June 2007. doi:10.2514/6.2007-4232

[11] Healy, J., "An Inverse Problem for Vertical-Axis Wind Turbines," *Journal of Energy*, Vol. 2, No. 6, 1978, pp. 382–384. doi:10.2514/3.47990

[12] Vandenberghe, D., and Dick, E., "Optimum Pitch Control for Vertical Axis Wind Turbines," *Wind Engineering*, Vol. 11, No. 5, 1987, pp. 237–247.

[13] Rathi, D., "Performance Prediction and Dynamic Model Analysis of Vertical Axis Wind Turbine Blades with Aerodynamically Varied Blade Pitch," M.S. Thesis, North Carolina State Univ., Raleigh, NC, 2012. doi:1840.16/8079

[14] Brulle, R., "McDonnell 40kW Giromill Wind System, Phase 2: Fabrication and Test," Tech. Rept. RFP-3304, McDonnell Aircraft Corp., St. Louis, MO, June 1980.

[15] Erickson, D., Wallace, J., and Peraire, J., "Performance Characterization of Cyclic Blade Pitch Variation on a Vertical Axis Wind Turbine," *49th AIAA Aerospace Sciences Meeting*, AIAA Paper 2011-0638, Jan. 2011. doi:10.2514/6.2011-638

[16] Adams, Z., and Chen, J., "Flux-Line Theory: A Novel Analytical Model for Vertical Axis Wind Turbines," *AIAA Journal*, Vol. 55, No. 11, 2017, pp. 3851–3867. doi:10.2514/1.J055804

[17] Madsen, H., and Lundgren, K., "The Voith–Schneider Wind Turbine: Some Theoretical and Experimental Results on the Aerodynamics of the Voith–Schneider Wind Turbine," Tech. Rept. NP-2900722, Inst. of Industrial Constructions and Energy Technology, Aslborg Univ. Centre, Aslborg, Denmark, 1980. doi:10.13140/RG.2.1.1725.8725

[18] Vandenberghe, D., and Dick, E., "A Theoretical and Experimental Investigation into the Straight Bladed Vertical Axis Wind Turbine with Second Order Harmonic Pitch Control," *Wind Engineering*, Vol. 10, No. 3, 1986, pp. 122–138.

[19] Jarugumilli, T., Lind, A., Benedict, M., and Lakshminarayan, V., "Experimental and Computational Flow Field Studies of a MAV-Scale Cycloidal Rotor in Forward Flight," *Proceedings of the 69th Annual Forum*, American Helicopter Soc., Fairfax, VA, 2013.

[20] Farrell, P., and Maddison, J., "Conservative Interpolation Between Volume Meshes by Local Galerkin Projection," *Computer Methods in Applied Mechanics and Engineering*, Vol. 200, Nos. 1–4, 2011, pp. 89–100. doi:10.1016/j.cma.2010.07.015

[21] Issa, R., "Solution of the Implicitly Discretised Fluid Flow Equations by Operator-Splitting," *Journal of Computational Physics*, Vol. 62, No. 1, 1986, pp. 40–65. doi:10.1016/0021-9991(86)90099-9

[22] Chowdhury, A., Akimoto, H., and Hara, Y., "Comparative CFD Analysis of Vertical Axis Wind Turbine in Upright and Tilted Configuration," *Renewable Energy*, Vol. 85, Jan. 2016, pp. 327–337. doi:10.1016/j.renene.2015.06.037

[23] Hansen, K., Barthelmie, R., Jensen, L., and Sommer, A., "The Impact of Turbulence Intensity and Atmospheric Stability on Power Deficits due to Wind Turbine Wakes at Horns Rev Wind Farm," *Wind Energy*, Vol. 15, No. 1, 2012, pp. 183–196. doi:10.1002/we.v15.1

[24] Benedict, M., "Fundamental Understanding of the Cycloidal-Rotor Concept for Micro Air Vehicle Applications," Ph.D. Thesis, Univ. of Maryland, College Park, MD, 2010.

[25] Soraghan, C., Leithead, W., Yue, H., and Feuchtwang, J., "Double Multiple Streamtube Model for Variable Pitch Vertical Axis Wind Turbines," *31st AIAA Applied Aerodynamics Conference*, AIAA Paper 2013-2802, 2013. doi:10.2514/6.2013-2802

[26] Islam, M., Ting, D., and Fartaj, A., "Aerodynamic Models for Darrieus-Type Straight-Bladed Vertical Axis Wind Turbines," *Journal of Renewable and Sustainable Energy*, Vol. 12, No. 4, 2008, pp. 1087–1109. doi:10.1016/j.rser.2006.10.023

[27] Leishman, G., *Principles of Helicopter Aerodynamics*, Cambridge Univ. Press, New York, 2006, pp. 427–429.

[28] Akimoto, H., Hara, Y., Kawamura, T., Nakamura, T., and Lee, Y., "A Conformal Mapping Technique to Correlate the Rotating Flow Around a Wing Section of Vertical Axis Wind Turbine and an Equivalent Linear Flow Around a Static Wing," *Environmental Research Letters*, Vol. 8, No. 4, 2013, Paper 044040. doi:10.1088/1748-9326/8/4/044040

[29] Bouton, I., "Lift-Curve Slope for Swept and Unswept Wings," *Journal of the Aeronautical Sciences*, Vol. 17, No. 3, 1950, p. 185. doi:10.2514/8.1573

[30] Adams, Z., Benedict, M., Hrishikeshavan, V., and Chopra, I., "Design, Development, and Flight Test of a Small-Scale Cyclogyro UAV Utilizing a Novel Cam-Based Passive Blade Pitching Mechanism," *International Journal of Micro Air Vehicles*, Vol. 5, No. 2, 2013, pp. 144–162. doi:10.1260/1756-8293.5.2.145

[31] Wilson, R., Shepherd, D., Spera, D., Divone, L., Thresher, R., Robinson, M., Musial, W., Veers, P., Viterna, L., Ancona, D., Schreck, S., Lissaman, P., Hubbard, H., Shepherd, K., Frost, W., Aspliden, C., Sengupta, D., Senior, T., Doman, G., Thresher, R., Mirandy, L., Carne, T., Lobitz, D., James, G., Ancona, D., Weinberg, C., and Wright, A., *Wind Turbine Technology*, ASME Press, New York, 2009, pp. 281–350.

F. N. Coton
Associate Editor